2018

The Effect of Martensite-Fractions Assumptions In Shape Memory Alloy Springs

Christian Vazquez

STARS Citation

Vazquez, Christian, "The Effect of Martensite-Fractions Assumptions In Shape Memory Alloy Springs" (2018). *Electronic Theses and Dissertations, 2004-2019*. 6203.
https://stars.library.ucf.edu/etd/6203

THE EFFECT OF MARTENSITE-FRACTIONS ASSUMPTIONS IN SHAPE MEMORY ALLOY SPRINGS

by

CHRISTIAN VAZQUEZ
B.S. University of Central Florida, 2017

A thesis submitted in partial fulfilment of the requirements
for the degree of Master of Science in Aerospace Engineering
in the Department of Mechanical and Aerospace Engineering
in the College of Engineering and Computer Science
at the University of Central Florida
Orlando, Florida

Fall Term
2018

Major Professor: Jeffrey L. Kauffman

ABSTRACT

This research addresses various models of a spring-mass system that uses a spring made of a shape memory alloy (SMA). The system model describes the martensite fractions, which are values that describe an SMA's crystalline phases, via differential equations. The model admits and this thesis contrasts two commonly used but distinct assumptions: a homogeneous case where the martensite fractions are constant throughout the spring's cross section, and a bilinear case where the evolution of the martensite fractions only occurs beyond some critical radius. While previous literature has developed a model of the system dynamics under the homogeneous assumption using the martensite-fractions differential equations, little research has focused on the dynamics when considering the bilinear case, especially using the differential equations. This thesis models the system dynamics under both the homogeneous and bilinear assumptions and determines if the bilinear case is an improvement over the homogeneous case. The research develops a numerical approach of the system dynamics for both martensite-fractions assumptions. For various initial displacements and temperatures, plotting the resulting displacement, velocity, and martensite fractions over time determines the coherence of the assumptions. Not only did the bilinear assumption offer more reasonable plots, but the homogeneous assumption delivered bizarre results for certain temperatures and initial displacements. For future research, a fully nonlinear case can replace the homogeneous and bilinear assumptions. Additionally, future research can utilize other martensite-fractions evolution models, as opposed to differential equations.

ACKNOWLEDGMENTS

Words cannot express how much I appreciate the efforts of my advisor, Dr. Jeffrey L. Kauffman. Not only has he helped me with developing my thesis, but he has also offered guidance throughout my graduate career, and has cared for my growth as an academic, engineer, and well-balanced person.

I would like to thank Dr. Tuhin Das and Dr. Kawai Kwok for agreeing to be a part of the committee for my thesis defense, and for listening to what I have been conducting research during the past year or so.

Lastly, I would also like to thank my friends and family, since your prayers and advice are much appreciated. My family, particularly my parents and brother, have molded me into the man I am today, showing me that I should obtain knowledge and wisdom. My friends have also supported and have reminded me of the joy of being in the presence of others.

TABLE OF CONTENTS

LIST OF FIGURES

LIST OF TABLES

CHAPTER 1: INTRODUCTION

In their most basic definition, smart and adaptive structures are a class of materials that exhibit a response due to an external stimulus. This definition is intentionally broad and all-encompassing because of the wide variety of adaptive structures, each with different stimuli and responses. With extensive research within the past half-century, these structures have shifted from being viewed as novelties to parts of real engineering systems [1]. The focus of this thesis is on one particular group of smart and adaptive structures: shape memory alloys (SMAs). SMAs exhibit one-way thermomechanical coupling, which means that SMAs can be heated to achieve some sort of displacement, but the reverse operation of obtaining heat from a change in displacement does not work. SMAs possess an intriguing trait; an SMA can be "trained" to a certain position or shape, such that when it is significantly deformed, it can return to its "trained" shape when heated. Due to this unique property, SMAs have many benefits over traditional systems, chief among them that systems that incorporate SMAs typically weigh less than other systems that do not include SMAs, a feature that is beneficial for space applications where the weight of items is crucial [2]. This chapter explores some of the fundamental ideas behind SMAs, as well as their applications in engineering systems.

Shape Memory Alloys

There are several important concepts to know regarding the fundamental mechanics of an SMA. One of these concepts is that of phase transformations. When an SMA is deformed or restored to its "memorized" position, the crystalline structure of the SMA changes. The two main phases are austenite and martensite. The crystalline makeup in the austenite phase is characterized by stacked rectangles. The martensite phase is similar, only the cells resemble rhombi as opposed to rectangles. The martensite phase is further classified into twinned and detwinned martensite. The lattice for detwinned martensite has the cells oriented in the same direction, while the twinned counterpart's lattice has the rhombi facing opposite directions. Figure 1.1 illustrates the various crystalline structures [3].

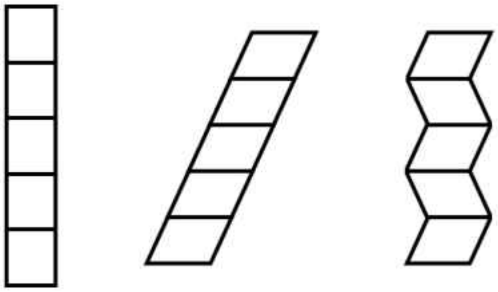

Figure 1.1: Austenite, Detwinned Martensite, and Twinned Martensite Phases

The phase transformation can be measured via a nondimensional value called the martensite fraction, typically denoted by ξ or β. When an SMA is in the austenite phase, the martensite fraction is $\xi = 0$. Conversely, $\xi = 1$ when an SMA is fully martensite. The detwinned and twinned martensite phases are also denoted by their own variables, and their sum is ξ. Other researchers use other models with different variables and more than two martensite fractions. Despite other models and any differences in notation, the most important property regarding martensite fractions is that they must have a value between zero and one.

A good grasp of crystalline phases and martensite fractions is crucial to an understanding of SMA effects. SMAs can undergo one of two different effects. The first of these is the shape memory effect. In this path, the SMA is configured into a desired shape and heated such that the material "memorizes" this configuration. The SMA is then deformed to a different shape. Finally, the SMA is heated again, this time returning to the shape that it "remembered". The pseudoelastic effect is the other path. Here, the SMA is also deformed (well beyond its elastic limit), but the SMA will return to its original shape, demonstrating pseudoelasticity.

These two effects are best understood by studying their stress-strain curves, which are highly nonlinear. For the following examples, it is assumed that the SMA has already "memorized" a desired shape and is initially in the austenite phase (i.e., $\xi = 0$). Examining the shape memory effect first, with its stress-strain curve shown in Fig. 1.2, the SMA starts at point A with neither applied stress nor strain. The SMA is then loaded elastically till it reaches its critical stress at point B. From point B, the SMA continues to be loaded until the SMA is fully in the martensite phase (i.e., $\xi = 1$) at point C. The material is then unloaded elastically until there is no more applied stress at point D. Note that at point D, there remains a residual strain. Finally, the SMA is heated till it returns to its pre-set configuration in the austenite phase, arriving at point E, which is also point A [4].

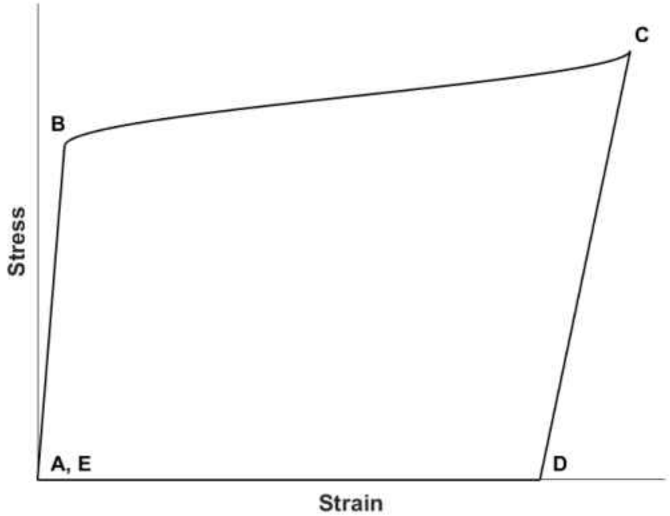

Figure 1.2: Typical Stress-Strain Curve for the Shape Memory Effect

Examining the pseudoelastic effect in Fig. 1.3, the processes from points A to B and points B to C are the same as in the pseudoelastic effect. From point C, the SMA is unloaded, again elastically, until the unloading process reaches a limit, demarcated as point D. The SMA continues unloading until it returns to the austenite phase at point E. Note that the process from points D to E required no temperature input [4].

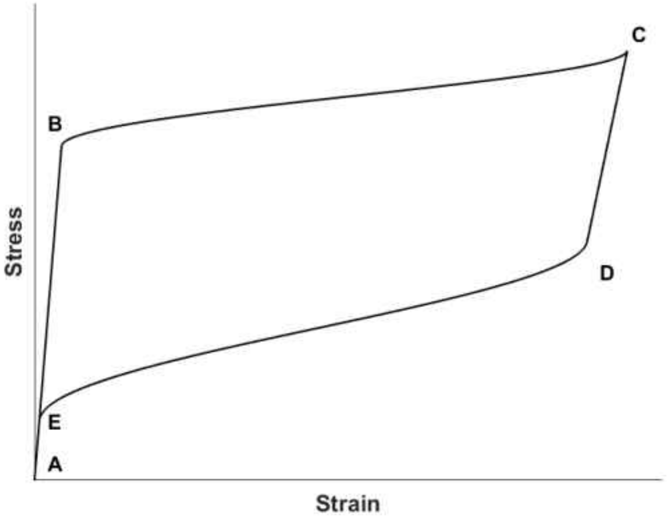

Figure 1.3: Typical Stress-Strain Curve for the Pseudoelastic Effect

Note that the slopes of the stress-strain curve between loading processes $A \rightarrow B$ and $C \rightarrow D$ are not identical. This phenomenon is the result of each phase having different values of the modulus of elasticity. Equation 1.1 shows a simple equation that models these different moduli, where E is the current modulus of elasticity, while E_A and E_M are the moduli of elasticity when an SMA is purely austenite and martensite, respectively. If $\xi = 0$, then $E = E_A$. On the other hand, $E = E_A$ when $\xi = 1$. The previous two moduli values can be thought of as limits for the modulus of elasticity at any given time. The model shown in Eq. 1.1 highlights the importance of keeping the martensite fraction between zero and one;

if the value of the martensite fraction is not in this range, then the equation will offer an unrealistic and nonsensical result [5].

$$E = E_A + \xi \left(E_M - E_A \right) \tag{1.1}$$

One final concept to note is the relationship between temperature and critical stress (the stress at the points A, B, C, D, and E in Fig. 1.2 and Fig. 1.3). This relationship is demonstrated by the plot in Fig. 1.4. There are four main temperatures to consider: the martensite finish temperature M_f, martensite start temperature M_s, austenite start temperature A_s, and austenite finish temperature A_s. These four temperatures are denoted by red dashed lines in Fig. 1.4. The black lines represent critical stress values, and phase transformations occur in the areas between the black lines. Notice that with the exception of the martensite finish temperature M_f, the critical stresses are not constant past the temperatures M_s, A_s, and A_f, and are instead temperature dependent. This graph reveals that if the stress were held constant, phase transformations can occur if the temperature is raised or lowered. Similarly, phase transformations can also occur at a constant temperature if the SMA is loaded or unloaded [6].

Aside from the transformation temperatures, there are also a few more key values to extract from Fig. 1.4 as well. Two important parameters to obtain are the martensite start and finish minimum critical stresses, which are, respectively, the top and bottom horizontal lines in Fig. 1.4. They are denoted by $\sigma_s^{\min}$ and $\sigma_f^{\min}$ [6]. Two other variables are the slopes of the martensite and austenite transformations, denoted by C_M and C_A, respectively, which are experimentally defined [7]. With these values defined, the critical stresses at any temperature can now be defined. Of particular importance to this thesis is the martensite start critical stress, which is highlighted below in Eq 1.2.

$$\sigma_s^{\text{crit}} = \sigma_s^{\min} + C_M \left(T - M_s\right) \tag{1.2}$$

The other critical stress equations are similarly constructed in light of Eq. 1.2, especially upon further examination of Fig. 1.4.

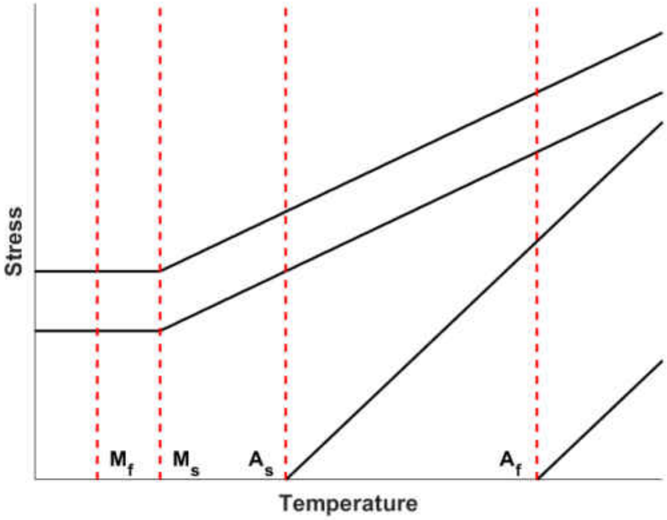

Figure 1.4: Typical Stress-Temperature Plot

Shape Memory Alloy Applications

SMAs are integrated in many engineering systems. In aviation, Mabe, Calkins, and Alkislar incorporated SMAs on a commercial airplane's jet nozzle to control the nozzle's size and thus affect noise production and fuel consumption. The authors created a miniature-scale model of the nozzle where the SMAs were configured in an antagonistic fashion to control the expansion and contraction of the nozzle. Their results indicated that expanding the nozzle area led to a decrease in noise. Additionally, the control system utilized kept the nozzle diameter at their desired areas over a long period of time [8]. In another paper, Tawfik, Ro, and Mei researched the effect of embedding SMAs into a panel that could be found on aerospace vehicles. Their research involved discovering how integrating SMAs could influence the buckling characteristics of the panel, as well as identifying a relationship between SMAs and panel fluttering. The researchers noticed that the embedded panel not only buckled at significantly greater temperatures, as opposed to a normal panel, but the embedded panel also reported less deflection once buckling occurred. As for flutter, the critical dynamic pressure past which flutter occurs rises considerably for panels with SMAs embedded in them. Part of this research was also concerned with determining the trade-off between better buckling properties and partially embedding the panel (over weight concerns), with the authors understanding that trade-offs are applied on a case-by-case basis [9].

There are also civil engineering applications for SMAs. Li, Liu, and Ou, conducted an investigation on the addition of SMA dampers to cables on cable-stayed bridges. The authors modeled the cables as beams clamped at both ends (with the SMA damper added some distance down the beam), and obtained a closed-form solution of the beam's deflection for the first mode as a function of the distance from one end and time using the Galerkin method. They also numerically solved for the deflection for modes beyond the first mode, and compared all of the deflections to a case without any SMA control. In all cases, there was greater damping when the SMA damper was added than without the damper. Also, the damping was found to be greatest when the damper was placed at certain points on the beam. For example, when the SMA damper was attached at 20% of the beam's length, the first mode experienced the greatest damping [10]. In a paper by Sakai et al., the effect of adding SMAs to a concrete slab was examined. The SMAs were added to the concrete much like a rod of rebar. The test consisted of applying a load at the middle of the slab until the concrete broke, and then the concrete was unloaded to see just how much the SMAs brought the slab to its original shape through the pseudoelastic effect. Sakai et al. reported that many cases, the SMAs, once unloaded, were able to return to approximately a tenth of its maximum deflection when it was completely loaded. The authors' hope was to help a building and its structures retain its shape after natural disasters like earthquakes [11].

Finally, there are uses for SMAs within the field of medicine as well. Pittaccio and Viscuso created a device that includes SMAs which helps patients flex their ankles for rehabilitation purposes. The investigators had healthy individuals undergo a couple of tests wearing the orthosis on their feet. The purpose of the tests was to analyze a passive control system where the device would flex the subject's foot and an active system that gives the patient a certain degree of autonomy in moving their ankle. The authors were able to show significant angular deflection (up to 40°) in the subjects' feet when wearing the device, as well as a significant resisting torque produced by the SMA actuators. While large angles were certainly promising, the researchers saw merit in even producing smaller angles, as these smaller angles are typically observed when people are walking [12].

Of the many diverse uses listed above, SMAs are used in two main ways. The first way they are used is as an actuator. Figure 1.5 demonstrates a model of an SMA actuator, as described by Liang and Rogers [13]. As the SMA is heated, the attached mass will want to travel in one direction or the other, depending on the "memorized" position of the SMA. As the mass is pulled or pushed, the spring will compress or extend accordingly. Finally, the mass will return to its original position when the SMA is cooled and the stored spring energy is released. Of course, the SMA and spring constitutes but one design. Liang and Rogers also mention a system similar to Fig. 1.5, but the spring is replaced with another SMA [13].

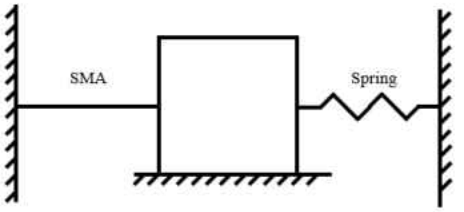

Figure 1.5: An SMA Actuator

The other interesting application of SMAs is their use as springs, the focus of this thesis. When configured in a system like Fig. 1.6, the system exhibits inherent damping without the use of external dampers. Lagoudas, Kalmár-Nagy, and Lagoudas observe better damping results from a system with an SMA spring than from a normal spring acted upon by friction alone [14]. This damping is the result of the changing phases, which affect the modulus of elasticity. Therefore, the way SMA springs damp is akin to state switch damping with piezoelectric materials. What helps with modeling SMA springs is that they are modeled similarly to regular springs. Therefore, it is worth briefly mentioning some basic spring concepts.

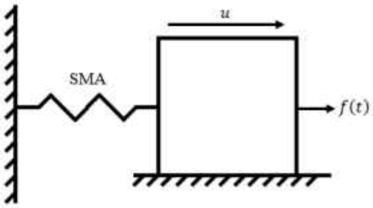

Figure 1.6: SMA-Spring-Mass System

Consider a spring with N coils, diameter D, and wire diameter d, like the one shown in Fig. 1.7. A shear force F acts on the spring in the direction of the longitudinal displacement u, as well as a torsion T. Using Castigliano's theorem, the spring constant k can be calculated.

Some important assumptions when using Castigliano's will be listed. The first of these is that the torsion is a function of the shear force. The next assumption is that the contribution of just the shear force to the strain energy is negligible. Finally, the material used to fabricate the spring is isotropic, such that the shear modulus G can be solved using the modulus of elasticity and Poisson's ratio. These assumptions result in Eq. 1.3 [15].

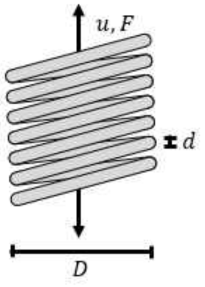

Figure 1.7: Typical Spring

$$k = \frac{Gd^4}{8D^3N} \tag{1.3}$$

Note here that the spring constant, as the name implies, is constant for a typical material. For an SMA, however, the changing modulus, as seen in Eq. 1.1, results in a varying value of k. With the spring constant defined, the restoring force of a spring can be examined briefly as well. Assuming a spring is perfectly linear, the restoring force can be modeled using Hooke's law, $F = ku$, where u is the system displacement. Examining Fig. 1.6, the differential equation describing the motion of the system is reflected by Eq. 1.4, where m is the mass of the attached block, c the external damping coefficient, and $f(t)$ the applied force. For a typical spring, the restoring force, as seen before, is a function of only the displacement. For an SMA spring, however, the restoring force is not only a function of the displacement, but also any martensite fractions and the temperature of the spring.

$$m\ddot{u} + c\dot{u} + F = f\left(t\right) \tag{1.4}$$

Problem Statement and Thesis Structure

When modeling the dynamics of an SMA-spring-mass system, there are a few philosophies of how the martensite fractions evolve within an SMA wire. One of these assumptions is a homogeneous assumption, where the martensite fractions' variation is constant throughout the SMA wire cross section. While this assumption may be sufficient for some engineering applications, this martensite-fractions assumption is not entirely realistic. By assuming another martensite-fractions variation across the wire cross section, numerical calculations may offer more accurate solutions. If researchers can better determine the system response and stress state, companies can design SMA springs to achieve a desired damping ratio for their projects, or justify the use of an SMA spring over a traditional spring that damps via friction or external dampers.

There is other research that focuses on modeling the dynamics of an SMA-spring-mass system. Aguiar, Savi, and Pacheco assumed a homogeneous distribution of the martensite fractions for their numerical solution. Additionally, the phase transformations are represented by differential equations. Their calculations and experimental findings, however, were for a system where there was an applied mechanical and thermal load that would vary throughout the experiment [16]. In another paper, de Sousa, De Marqui Junior, and Elahinia split the SMA wire's cross section into several annular rings, preferring a non-homogeneous assumption instead. There numerical solution, however, described the evolution of the martensite fractions through an experimental model that does not use differential equations [17]. The goal of this study is to consider another modeling alternative: a non-homogeneous martensite-fractions assumption where differential equations determine the evolution of the martensite fractions. A single degree of freedom system like in Fig. 1.6 will be considered under free vibrations, and key items like the system's displacement, velocity, and martensite fractions will be obtained using a bilinear case (i.e., separating the cross-section into two annular rings). Using these differential equations, the aforementioned variables will also be derived for the homogeneous case, and the values from each case will be compared. The purpose of the comparison is to see if the two distributions vary significantly, and if so, determine if the bilinear case is an improvement over the homogeneous case.

This thesis will be organized in the following manner. The second chapter reviews the current literature, particularly on the development of the current constitutive SMA and shear stress models, and how to expand the current research. Chapter three examines the numerical methods needed to model SMA-spring-mass system dynamics. The results and the interpretation of these results are given in the fourth chapter. The final chapter offers a conclusion of this thesis and highlights a plan for future work.

CHAPTER 2: LITERATURE REVIEW

The equations, concepts, and methods mentioned in the third chapter have an extensive history. This chapter will explore that history, particularly the development of the martensite-fractions evolution and the stress experienced within an SMA.

Martensite-Fractions Model

While there are many different martensite-fractions models to describe SMAs, two different models will be highlighted in this thesis: the experimental model and the differential model. The models are quite different from one another. The experimental model consists of one martensite fraction that is updated whenever there is a change in the phase (i.e., $A \rightarrow M$ to $M \rightarrow A$ and vice versa). The differential model, as opposed to the one dimensional model, describes the dynamics of several martensite fractions via differential equations. These models will be expanded upon in greater detail.

Experimental Model

One of the first models to described the one-dimensional phase transformation of SMAs was one developed by Tanaka and Nagaki. In order to describe the phase transformation, they adopt an exponential law, as seen by Eq. 2.1 and Eq. 2.2 [18].

$$\xi_{M\rightarrow A} = e^{[A_a(T-A_s)+B_a\sigma]} \tag{2.1}$$

$$\xi_{A\to M} = 1 - e^{[A_m(T-M_s)+B_m\sigma]} \tag{2.2}$$

There are some important features to highlight in these equations. First, the martensite fraction is a function of both temperature T and stress σ. Also note that in this model, the phase transformation is only one way. That is, Eq. 2.1 can only go from martensite to austenite, and never go in the opposite direction. If an austenite to martensite phase transformation is desired, then Eq. 2.2 must be used instead. One final element of the model to highlight is that these equations assume that the SMA is fully changing from one phase to the other, and does not account for incomplete phase transformations [18].

Liang and Rogers take a different approach in defining the phase transformation. Rather than defining the phase transformations using an exponential law, the authors use a cosine law. Equation 2.3 and Eq. 2.4 describe this cosine law [19].

$$\xi_{A\to M} = \frac{\xi_0}{2}\left\{\cos\left[a_A\left(T-A_s\right)-\frac{a_A}{C_A}\sigma\right]+1\right\} \tag{2.3}$$

$$\xi_{M\to A} = \frac{1-\xi_0}{2}\cos\left[a_M\left(T-M_f\right)-\frac{a_M}{C_M}\sigma\right]+\frac{1+\xi_0}{2} \tag{2.4}$$

where ξ_0 is the initial value of the martensite fraction before a transformation occurs in either direction. In this model, an initial martensite fraction is introduced to account for incomplete phase transformations. Note, however, that ξ_0 is not the same value for both Eq. 2.3 and Eq. 2.4, but is rather the initial martensite fraction given that the phase transformation is changing in a certain way.

Brinson added to Liang and Roger's model by incorporating different types of martensite. Brinson distinguishes between temperatured-induced martensite ξ_T and stress-induced martensite ξ_S (analogous to twinned and detwinned martensite, respectively). These martensite fractions are related to ξ through Eq. 2.5 [20].

$$\xi = \xi_S + \xi_T \tag{2.5}$$

With a difference in martensite fractions now, the model must now be updated. Brinson separates the model into three segments. The first segment, illustrated by Eq. 2.6 and Eq. 2.7, describes the martensite fraction when under the conditions $T > A_s$ and $C_A\left(T - A_s\right) < \sigma < C_A\left(T - A_f\right)$ (i.e., the transformation from martensite to austenite) [20].

$$\xi = \frac{\xi_0}{2}\left\{\cos\left[a_A\left(T - A_s - \frac{\sigma}{C_A}\right)\right] + 1\right\} \tag{2.6}$$

$$\xi_S = \xi_{S0} - \frac{\xi_{S0}}{\xi_0}\left(\xi_0 - \xi\right) \tag{2.7}$$

where ξ_T can be solved using Eq. 2.5. Austenite to martensite transformations are described by two conditions. Under the first condition, $T < M_s$ and $C_A\left(T - A_s\right) < \sigma < C_A\left(T - A_f\right)$ $\sigma_s^{\text{crit}} + C_M\left(T - M_s\right) < \sigma < \sigma_f^{\text{crit}} + C_M\left(T - M_s\right)$, Eq. 2.8 and Eq. 2.9 give the evolution for stress- and temperature induced martensite.

$$\xi_S = \frac{1 - \xi_{S0}}{2}\cos\left\{\frac{\pi}{\sigma_s^{\text{crit}} - \sigma_f^{\text{crit}}}\left[\sigma - \sigma_f^{\text{crit}} - C_M\left(T - M_s\right)\right]\right\} + \frac{1 + \xi_{S0}}{2} \tag{2.8}$$

$$\xi_T = \xi_{T0} - \frac{\xi_{T0}}{1-\xi_{S0}}\left(\xi_S - \xi_{S0}\right) \tag{2.9}$$

Differential Model

One of the earliest free energy equations to be developed was by Fremond [21], which is comprised of the normal strain ε, a rigidity matrix, and few other parameters with regard to temperature. Fremond proposed a model where there exist three different martensite fractions, one associated with austenite and the other two associated with martensite. The martensite fractions, denoted by the variable β, have two properties. The first property is that each martensite fraction must have a value between 0 and 1. The other property is that the sum of the martensite fractions at all times must equal 1. These two criteria are summarized below in Eq. 2.10 and Eq. 2.11.

$$0 \leq \beta_i \leq 1 \tag{2.10}$$

$$\sum \beta_i = 1 \tag{2.11}$$

where i is the number martensite fraction, which in Fremond's research is $i = 3$. With the constraint provided by Eq. 2.11, β_3 can be eliminated from the free energy equation, and can therefore be written in terms of β_1 and β_2. The reasons for eliminating β_3 from the free energy equation are twofold. One of these reasons is that from the free energy equation, thermodynamic stresses can be derived for β_1 and β_2 by taking the partial derivative of the free energy equation with respect to β_1 and β_2. The other reason is to define the indicator function $TI(\beta_1, \beta_2)$ in terms of two fractions instead of three, as seen in Eq. 2.12 [21]. This indicator function ensures that the martensite-fractions criteria in Eq. 2.10 and Eq. 2.11 are met at all times. This indicator function can also be visualized as a triangle on a coordinate plane, like in Fig. 2.1, where β_1 and β_2 must be inside the shaded triangle at all times. If the coordinate (β_1, β_2) is not within the triangle, then a law (visualized by the dashed lines in Fig. 2.1) forces the coordinate back to the edges of the triangle. With β_1 and β_2 solved and corrected as needed, β_3 is easily defined using Eq. 2.11. The partial derivatives of the indicator function, known as sub-differentials, are also taken with respect to β_1 and β_2 and added to the thermodynamic stresses.

$$\mathcal{F} = \{(\beta_1, \beta_2) \, | 0 \leq \beta_i \leq 1; \beta_1 + \beta_2 \leq 1\} \tag{2.12}$$

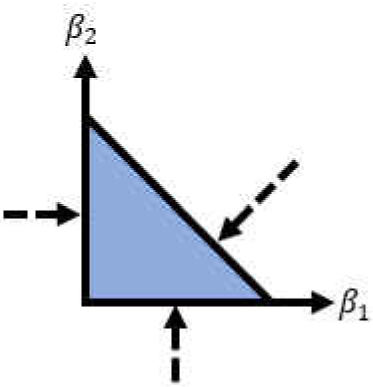

Figure 2.1: Two Dimensional Fraction Constraint Law

Another development in the martensite-fractions model was the introduction of Lagrange multipliers into the indicator function by Savi and Braga [22]. The constraints from Eq. 2.10 and Eq. 2.11 are rewritten so that the right hand side is ≤ 0 (e.g., $\beta_1 + \beta_2 \leq 1$ becomes $\beta_1 + \beta_2 - 1 \leq 0$). The constraint equations are then multiplied by Lagrange multipliers λ_i.

Equation 2.13 illustrates the changes in the indicator function.

$$I = -\lambda_1\beta_1 - \lambda_2\beta_2 + \lambda_3\left(\beta_1 + \beta_2 - 1\right) \tag{2.13}$$

Note that the upper bound $\beta_i \leq 1$ has vanished, since the constraint $\beta_i \geq 0$ coupled with $\beta_1 + \beta_2 \leq 1$ inherently sets an upper limit of 1. With these Lagrange multipliers and constraint equations, the sub-differentials can easily be derived and added to the thermodynamic stresses.

Savi and Braga make another development to the model. One important assumption is that the thermodynamic stresses developed in [21], which usually account for normal parameters, are modified to incorporate shear parameters instead. Differential equations for β_1 and β_2 are then derived from the thermodynamic stresses. Equation 2.14 gives the differential equations that describes the dynamics of the martensite fractions, where, η_i is a dissipation factor.

$$\eta_i\dot{\beta}_i = B_i \tag{2.14}$$

The next development in the martensite-fractions evolution is brought by Paiva, Savi, Braga, Baêta-Neves, and Pacheco through several papers. The authors add a fourth martensite fraction to the model. The first two fractions are still related to martensite (although they now specifically refer to detwinned martensite) and the third still to austenite. The fourth fraction is also related to martensite, but it refers to twinned martensite. The indicator function expressed in Eq. 2.12 and Eq. 2.13 now includes the expression $-\beta_3 \leq 0$, and the constraint $\beta_1 + \beta_2 - 1 \leq 0$ is now $\beta_1 + \beta_2 + \beta_3 - 1 \leq 0$. This indicator function, now called J_π, is listed in Eq. 2.15. The triangle in Fig. 2.1 is now updated to a three-dimensional tetrahedron like the one in Fig. 2.2. Once the constraint laws have been implemented and β_1, β_2, & β_3 solved, β_4 can be solved using Eq. 2.11 [23, 24, 25, 26].

$$\pi = \{\beta_i \in \mathcal{R} | 0 \leq \beta_i \leq 1; \beta_1 + \beta_2 + \beta_3 \leq 1\} \tag{2.15}$$

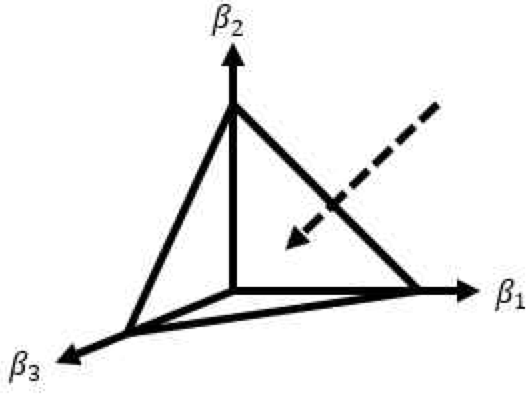

Figure 2.2: Three Dimensional Constraint law for J_π

Paiva, Savi, Braga, and Pacheco added another indicator function to the model, J_χ. The indicator function J_χ is a constraint law that corrects $\dot{\beta}_i$, as opposed to β_i. The physical interpretation of J_χ is that it is concerned with internal sub-loops due to incomplete phase transformations. Equations 2.16 illustrates the indicator function for normal stresses σ and strains ε [25, 26].

$$
\begin{gathered}
\varepsilon_0 = \varepsilon - \frac{\Omega}{E}\left(T - T_0\right) \\
\dot{\sigma} \neq 0 \\
\chi = \left\{ \dot{\beta}_i \in \mathcal{R} \;\middle|\; \begin{array}{l} \dot{\varepsilon}\dot{\beta}_1 \geq 0;\quad \dot{\varepsilon}\dot{\beta}_3 \leq 0;\quad \text{if}\quad \varepsilon_0 > 0 \\ \dot{\varepsilon}\dot{\beta}_2 \leq 0;\quad \dot{\varepsilon}\dot{\beta}_3 \geq 0;\quad \text{if}\quad \varepsilon_0 < 0 \end{array} \right\} \\
\dot{\sigma} = 0 \\
\chi = \left\{ \dot{\beta}_i \in \mathcal{R} \;\middle|\; \begin{array}{c} \dot{T}\dot{\beta}_1 \begin{cases} < 0 & \text{if } \dot{T} > 0,\ \sigma < \sigma_M^{\text{crit}},\ \beta_1^s \neq 0 \\ = 0 & \text{otherwise} \end{cases} \\ \dot{T}\dot{\beta}_2 \begin{cases} < 0 & \text{if } \dot{T} > 0,\ \sigma < \sigma_M^{\text{crit}},\ \beta_2^s \neq 0 \\ = 0 & \text{otherwise} \end{cases} \\ \dot{T}\dot{\beta}_3 \geq 0 \\ -\dot{\beta}_1^2 - \dot{\beta}_1\dot{\beta}_3 = 0 \ \text{ or } \ -\dot{\beta}_2^2 - \dot{\beta}_2\dot{\beta}_3 = 0 \end{array} \right\}
\end{gathered}
\tag{2.16}
$$

where Ω is a thermal expansion coefficient, T_0 is a reference temperature, and the s superscript refers to the initial martensite fraction. There are some other assumptions made by Paiva, Savi, Braga, Baêta-Neves, and Pacheco. The modulus of elasticity changes value between the austenite and martensite moduli, similar to Eq. 1.1 (with β_3 replacing ξ). The previous assumption was to assume the modulus of elasticity as constant. Also, new parameters were introduced. of these terms, three will be highlighted. First are the terms related to critical stresses for phase transformations, exhibited in Eq. 2.17. The superscript S is a placeholder that depends on the martensite fraction; for β_1, β_2, and β_3, the superscript is T for tension for martensite phase transformations, C for compression for martensite transformations, and A for austenite transformations. Additionally, the martensite start temperature M_s is instead labeled T_M. [23, 24, 25, 26].

$$\Lambda_i = -L_0^S + \frac{L^S}{T_M}\left(T - T_M\right) \tag{2.17}$$

It is crucial to note that Λ_i is temperature dependent. The other two terms are related to the stress-strain hysteresis loop height α and width α_h, both of which have different values depending on whether the SMA is in tension or compression. One more assumption is that the dissipation parameter η_i changes value between an upper value U and lower value L, according to the inequality expressions in Eqs. 2.18 [24, 25, 26].

$$\begin{aligned} \eta_i &= \eta_i^L \ \text{ if } \ \dot{\varepsilon} > 0 \\ \eta_i &= \eta_i^U \ \text{ if } \ \dot{\varepsilon} < 0 \end{aligned} \tag{2.18}$$

The contribution Aguiar, Savi, and Pacheco made to the model was simplifying the differential equations derived in [23, 24, 25, 26]. Any values that had tension and compression components were assumed to be equal (e.g., $\alpha_h^T = \alpha_h^C = \alpha_h$). Additionally, all values other than Λ_i, α, and α_h were eliminated, so that for example, α_h is reduced to $\alpha_h = \gamma_R - \alpha/G_M$, where γ_R is the maximum residual strain. With these assumptions, Eq. 2.19, Eq. 2.20, and Eq. 2.21 are the martensite differential equations to be utilized in this thesis.

$$\dot{\beta}_1 = \frac{1}{\eta_1}\left[\left(\alpha + G\alpha_h\right)\gamma + \Lambda_1 + \left(2\alpha_h\alpha + G\alpha_h^2\right)\left(\beta_2 - \beta_1\right) - \partial_1 J_\pi\right] + \partial_1 J_\chi \tag{2.19}$$

$$\dot{\beta}_2 = \frac{1}{\eta_2}\left[-\left(\alpha + G\alpha_h\right)\gamma + \Lambda_2 - \left(2\alpha_h\alpha + G\alpha_h^2\right)\left(\beta_2 - \beta_1\right) - \partial_2 J_\pi\right] + \partial_2 J_\chi \tag{2.20}$$

$$\dot{\beta}_3 = \frac{1}{\eta_3}\left\{-\frac{1}{2}\left(G_A - G_M\right)\left[\gamma + \alpha_h\left(\beta_2 - \beta_1\right)\right]^2 + \Lambda_3 - \partial_3 J_\pi\right\} + \partial_3 J_\pi \tag{2.21}$$

Force

The development of the restoring force F begins with determining the equation for normal stress σ for SMAs. The equation for the normal stress was initially written as a differential equation, like in Eq. 2.22 [19].

$$\dot{\sigma} = E\dot{\varepsilon} + \Theta\dot{T} + \Omega\dot{\xi} \tag{2.22}$$

where E is the modulus of elasticity, Θ is a thermoelastic tensor, and Ω is a transformation tensor (the same Ω from Eq. 2.16). Integrating Eq. 2.22 with respect to time results in Eq. 2.23 [19].

$$\sigma - \sigma_0 = E\left(\varepsilon - \varepsilon_0\right) + \Theta\left(T - T_0\right) + \Omega\left(\xi - \xi_0\right) \tag{2.23}$$

Similarly, the normal stress was also derived for the differential model by Fremond. The stress tensor, which was derived by a free energy equation, is listed below in Eq. 2.24, where

$\mathbf{1}$ is the unity tensor and $\boldsymbol{K}$ is the rigidity matrix, similar to the modulus of elasticity [21].

$$\tilde{\sigma} = \alpha\left(\beta_2 - \beta_1\right)\mathbf{1} + \boldsymbol{K}\varepsilon \tag{2.24}$$

With an introduction to stresses, the restoring force is now presented. The restoring force of an SMA spring was first expressed as a torque by Tobushi and Tanaka. Equation 2.25 expresses this torque as a function of the shear stress [27].

$$M_t = \int_A \tau r^2 dA = 2\pi \int_0^{d/2} \tau r^2 dr \tag{2.25}$$

where r is the radial coordinate across the circular cross section of the SMA spring. Tobushi and Tanaka also mention that the restoring force and restoring torque are related through $M_t = FD/2$, assuming that the restoring force is a pure shear force [27]. This relation, along with Eq. 2.25, offers the solution of the restoring force, listed in Savi and Braga [22, 28]. Equation 2.26 displays the restoring force.

$$F = \frac{4\pi}{D} \int_0^{d/2} \tau r^2 dr \tag{2.26}$$

Savi and Braga assume that the normal stress developed by [21] is applicable to shear parameters (i.e., $E \to G$, $\sigma \to \tau$, $\varepsilon \to \gamma$, etc.), and simplify the stress tensor into a scalar. They also list the (normal) strain as a function of the radius [22]. With the aforementioned assumption of normal-to-shear analogs, the shear strain is now a function of the radius, with its equation presented in Eq. 2.27.

$$\gamma = \frac{2r}{\pi D^2 N} u \tag{2.27}$$

The scalar stress equation is updated by Paiva, Savi, Braga, and Pachecho in [23, 24, 25, 26] to accommodate the existence of another martensite fraction β_4. This stress equation is simplified by Aguiar, Savi, and Pachecho the same way the differential equations Eq. 2.19, Eq. 2.20, and Eq. 2.21 were simplified. In addition to an updated shear stress equation, demonstrated by Eq. 2.28, Aguiar, Savi, and Pacheco assume the existence of a critical radius r_T, which separates the cross section into two regions. The first region is the area under r_T, where there is no detwinned martensite (i.e., $\beta_1 = \beta_2 = 0$). Past the critical radius, $r_T < r \leq d/2$, detwinned martensite is present. Equation 2.29 presents the formulation of the critical radius [16]

$$\tau = G\gamma + (\alpha + G\alpha_h)(\beta_2 - \beta_1) \tag{2.28}$$

$$r_T = \frac{\pi D^2 N}{2Gu} \tau_{\text{crit}} \tag{2.29}$$

where τ_{crit} is the critical shear stress. With the critical radius defined, Eq. 2.26 can be integrated once more. Examining Eq. 2.28, the first term is dependent on neither β_1 nor β_2, so the lower integration bound remains at zero, and the term is integrated. The next term, however, does depend on β_1 and β_2, so the lower integration bound becomes r_T. Since the relationship between the radial coordinate and the martensite fractions remain unknown, the integrand is left in place, resulting in a fully non-linear restoring force in Eq. 2.30 [16].

$$F = \frac{\pi d^3}{8D}\left(\frac{d}{\pi D^2 N}G\right)u + \int_{r_T}^{d/2}\left(\alpha + G\alpha_h\right)\left(\beta_2 - \beta_1\right)r^2 dr \tag{2.30}$$

One assumption that can simplify the above equation is to assume that the martensite fractions are constant throughout the region $r_T < r \leq d/2$, resulting in a bilinear martensite-fractions case. Therefore, the integrand in Eq. 2.30 can be solved, resulting in Eq. 2.31.

$$F = \frac{\pi d^3}{8D}\left\{\left(\frac{d}{\pi D^2 N}G\right)u + \frac{4}{3}\left(\alpha + G\alpha_h\right)\left(\beta_2 - \beta_1\right)\left[1 - \left(\frac{2r_T}{d}\right)^3\right]\right\} \tag{2.31}$$

The last simplification to the model is to assume that the martensite fractions act through the entire cross section (i.e., $0 \leq r \leq d/2$). Mathematically, this is the same as assuming that $r_T = 0$. Inserting this condition into Eq. 2.31 gives Eq. 2.32.

$$F = \frac{\pi d^3}{8D}\left[\left(\frac{d}{\pi D^2 N}G\right)u + \frac{4}{3}\left(\alpha + G\alpha_h\right)\left(\beta_2 - \beta_1\right)\right] \tag{2.32}$$

For this thesis, the most recent research contribution to the restoring force was discovered by de Sousa, De Marqui Junior, and Elahinia. The shear critical stress τ_{crit} was assumed to be the critical shear martensite start stress. This is a reasonable assumption, since the region outside of the critical radius experiences a phase transformation from austenite to detwinned martensite. Since the temperature-stress plot only accounts for normal stresses, the critical shear stress must be calculated from the critical normal stress. Continuing with the pure shear assumption, the critical shear martensite start stress can be calculated using a von Mises approach to obtain $\sigma_s^{\text{crit}} = \sqrt{3}\tau_s^{\text{crit}}$, where σ_s^{crit} is obtained using Eq. 1.2 [17].

CHAPTER 3: MODEL DEVELOPMENT

This chapter will explore how to obtain the numerical solution to the system of differential equations. The goal is to obtain six plots: displacement and velocity versus time, a phase plot, the martensite fractions over time, the force-displacement plot, the shear stress as a function of the radius and time, and the critical radius for the bilinear case. This chapter begins by explaining how to solve for the displacement, and then the martensite fractions. Particular attention is given when studying the solution to the indicator functions. A flowchart at the end of the chapter summarizes the numerical solution.

It is paramount that the state variables of the system of differential equations be identified. From Eq. 1.4, the state variables are recognized as $x = [u\ \dot{u}\ \beta_1\ \beta_2\ \beta_3]^T$. Furthermore, the state variables will split into those relating to displacement and those relating to martensite fractions, such that the state vector is $x = [x_A\ x_B]^T$, where $x_A = [u\ \dot{u}]$ and $x_B = [\beta_1\ \beta_2\ \beta_3]$.

Before listing the solution to the system dynamics, several assumptions will be made that will simplify the problem. It is first assumed that the SMA is isotropic, such that Eq. 1.1, coupled with the Poisson's ratio, can be written with the shear modulus instead. The next assumption is that the temperature will be held constant during operation (i.e., $\dot{T} = 0$). Lastly, normal and shear values are interchangeable in the preceding equations (e.g., $E \to G$, $\varepsilon \to \gamma$).

Numerical Differential Equation Solution

The presence of the indicator functions complicates solving for the time response of the state variables. To solve the system of differential equations, the operator split technique is employed [29, 30]. As the name implies, this method consists of splitting the system of differential equations into multiple systems. In the case of this thesis, the system is split into the differential equations relating to the displacement, $\dot{x}_A$, and the differential equations relating to the martensite fractions, $\dot{x}_B$. When solving for one set of differential equations, the variables from the other set(s) are kept constant. Equations 3.1 highlights the split in the state variables [28].

$$\begin{aligned} \dot{x}_A &= f_A\left(x_A, x_B, t\right) \\ \dot{x}_B &= f_B\left(x_A, x_B, \lambda_{\pi,i}, \lambda_{\chi,i}, t\right) \end{aligned} \tag{3.1}$$

For any sets that have peculiar functions like the indicator functions for $\dot{x}_B$, those differential equations are further broken down into differential equations that do not include the peculiar functions and a correction that adds the peculiarities back into the equation. This second split is shown in Eqs. 3.2 [28].

$$\begin{aligned} \dot{x}_{B,1} &= f_{B,1}\left(x_A, x_B, t\right) \\ \dot{x}_{B,2} &= f_{B,2}\left(\lambda_{\pi,i}, \lambda_{\chi,i}\right) \end{aligned} \tag{3.2}$$

where the subscripts π and χ refer to the Lagrange multipliers tied to their respective indicator functions. Set A will be solved using a fourth order Runge-Kutta method, and set B will be solved using Euler's method. Eqs. 3.3 describe the numerical methods used [28].

$$\begin{aligned} x_A^{n+1} &= x_A^n + k_A^n \\ x_B^{n+1} &= x_B^n + \Delta t f_{B,1}\left(x_A, x_B, t\right) + \Delta x_\pi^n + \Delta x_\chi^n \end{aligned} \tag{3.3}$$

Here, k_A^n is the step solved by the fourth order Runge-Kutta that is added to the state variables x_A at each iteration of time. In the second equation in Eqs. 3.3, Δt is the time step for the numerical solution, and Δx_{π}^{n} & Δx_{χ}^{n} are the correction factors computed from the indicator functions J_{π} and J_{χ}, respectively.

Set A - Forcing Assumption

Set A of the differential equations, the displacement state variables $x_A = [u\ \dot{u}]$, shall be examined first. Of utmost importance when solving for x_A at each time step are the restoring force, expressed in Eq. 2.31, and the critical radius, featured in Eq. 2.29. As mentioned before, Eq. 2.31 simplifies to Eq. 2.32 when $r_T = 0$ in the homogeneous case, so solving for the displacement and velocity is fairly straightforward. However, for the bilinear case, an issue arises when Eq. 2.29 reports either a negative value or a value greater than the radius of the SMA wire, $d/2$, in which neither case makes physical sense. The first problem is resolved by solving the absolute value of the critical radius. Equation 3.4 reflects the update in the critical radius equation.

$$r_T = \left| \frac{\pi D^2 N}{2Gu} \tau_{\text{crit}} \right| \tag{3.4}$$

To solve the second issue, the critical radius will be reset to $r_T = d/2$ whenever Eq. 2.29 presents a value greater than the wire radius. Also, per the definiton of the critical radius—that stress-induced martensite always equals zero inside the critical radius—and the assumption that $\beta_4 = 0$ at all times, the martensite fractions are set to $\beta_1 = \beta_2 = 0$ and $\beta_3 = 1$.

Set B - Martensite Fractions

The evolution of the martensite fractions, which is much more involved and intriguing, will be explored next. The solution of the martensite fractions can be thought of in two regimes: pre-critical radius and post-critical radius, where pre-critical radius martensite fractions are calculated via the conditions mentioned at the end of the last section, and post-critical radius β_i's are solved via the differential equations. With the regimes in mind, there are three cases to consider. The first case is if the critical radius is the wire radius. In this case, there are no post-radius martensite fractions to compute, and the differential equations are altogether bypassed at that time step. The second case is when $r_T = 0$ (i.e the homogeneous assumption). The martensite fractions are all post-critical radius, and must therefore be solved by the differential equations. The last case is when $0 \leq r_T \leq d/2$ for a particular time step, where there will be both pre- and post-critical radius martensite fractions to consider. When the differential equation route is taken, Eq. 3.5 solves for Euler's method, where the bar above x_B^{n+1} represents the solution to only Euler's method without the inclusion of the indicator functions.

$$\overline{x}_B^{n+1} = x_B^n + \Delta t f_{B,1}\left(x_A, x_B, t\right) \tag{3.5}$$

The remainder of this section will examine the solution to post-critical radius β_i's. Although the initial solution to the martensite fractions is simple and straightforward, since they will be solved through Euler's method, the correction factors Δx_π and Δx_χ, as well as collecting the martensite fractions across each radius value, are of great interest.

Indicator Functions

Special attention is given to the indicator functions J_π and J_χ, particularly the solutions to Δx_π^n and Δx_χ^n from Eq. 3.3. The solution to $\partial_i J_\pi$ will be examined first. Consider again the triangular volume from Fig. 2.2. The volume can be split into four surfaces: a triangle on each of the coordinate planes in the β_1-β_2-β_3 axis (like in Fig. 2.1), and a fourth triangular surface connecting the three other surfaces. This split is useful in defining Δx_π^n, especially if one of the martensite-fractions differential equations offers a negative results. If, for example, β_3 happens to be negative, then a correction of $\Delta\beta_3 = -\beta_3$ (such that β_3 is corrected to equal zero) is employed and the other two martensite fractions can be corrected using a two dimensional triangle law. Savi and Braga defined the update for a two dimensional case [28] by separating the constraint triangle from Fig 2.1 into regions. Figure 3.1 reflects the updates in the triangular constraint law. From these regions, Savi and Braga define updates for β_1 and β_2, shown below in Table 3.1 for when $\beta_3 < 0$.

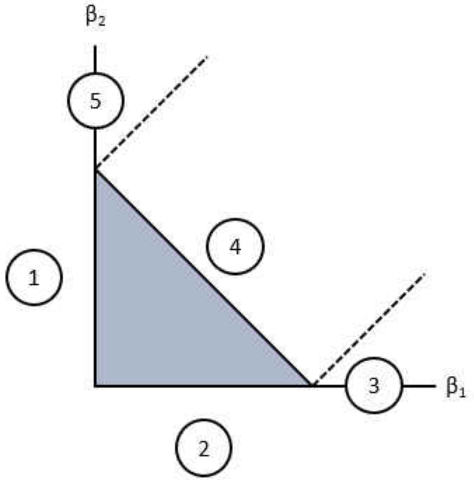

Figure 3.1: Two Dimensional Constraint Law for J_π

Table 3.1: Two Dimensional Constraint Law for J_π

Region	Constraint	$\Delta\beta_1$	$\Delta\beta_2$
Region 1	$\beta_1 < 0$	$-\beta_1$	0
Region 2	$\beta_2 < 0$	0	$-\beta_2$
Region 3	$\beta_2 \leq \beta_1 - 1$	$1 - \beta_1$	$-\beta_2$
Region 4	$\beta_2 > \beta_1 - 1$ & $\beta_2 < \beta_1 + 1$	$\frac{1-\beta_1-\beta_2}{2}$	$\frac{1-\beta_1-\beta_2}{2}$
Region 5	$\beta_2 \geq \beta_1 + 1$	$-\beta_1$	$1 - \beta_2$

A similar update law can be derived when β_1 or β_2 are less than zero instead of β_3. To obtain an update law for the entire three dimensional volume, the fourth face must be examined. This fourth face is also split into four regions, according to its three edges and the surface itself, visualized in Fig. 3.2. The dashed lines represent corrections that ensure the martensite fractions do not violate Eq. 2.11 (the circle with a cross is also a correction that goes into the page). The update law for the three dimensional volume is presented in Table 3.2. Note that the three dimensional law references the two dimensional law from Table 3.1. Also note that $i, j, k = 1, 2, 3$ for Region 4. With all of the corrections defined, the correction vector is calculated as $\Delta x_\pi^n = [\Delta\beta_1 \ \Delta\beta_2 \ \Delta\beta_3]^T$. The updated martensite fractions are reported in Eq. 3.6, where the double bar represents the martensite fractions calculated by Euler's method and the indicator function J_π.

$$\overline{\overline{x}}_B^{n+1} = \overline{x}_B^{n+1} + \Delta x_\pi^n \tag{3.6}$$

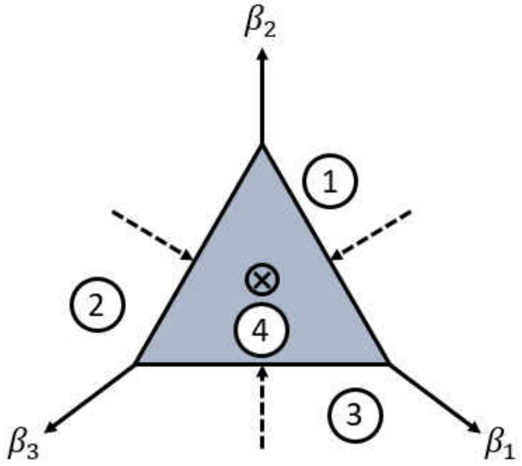

Figure 3.2: Constraint Law for J_π

Table 3.2: Three Dimensional Constraint Law for J_π

Region	Constraint	$\Delta\beta_1$	$\Delta\beta_2$	$\Delta\beta_3$
Region 1	$\beta_1 < \frac{\beta_2+\beta_3-1}{2}$	$-\beta_1$	2D	2D
Region 2	$\beta_2 < \frac{\beta_3+\beta_1-1}{2}$	2D	$-\beta_2$	2D
Region 3	$\beta_3 < \frac{\beta_1+\beta_2-1}{2}$	2D	2D	$-\beta_3$
Region 4	$\beta_k > \frac{\beta_i+\beta_j-1}{2}$	$\frac{1-\beta_1-\beta_2-\beta_3}{3}$	$\frac{1-\beta_1-\beta_2-\beta_3}{3}$	$\frac{1-\beta_1-\beta_2-\beta_3}{3}$

Now inspecting J_χ, the assumptions from the beginning of the chapter will be applied. Assuming constant temperature, the change in the martensite fractions will be a result of varying stress. The result of this assumption is that effect of J_χ when $\dot{\sigma} = 0$ is negligible, and can therefore be ignored. Also, the term ε_0 from Eq. 2.16 simplifies to $\varepsilon_0 = \varepsilon$ when temperature changes are ignored. If the interchangeability of normal and shear values is assumed, then Eq. 3.7 illustrates the updated and simplified J_χ.

$$\chi = \left\{ \dot{\beta}_i \in \mathcal{R} \;\middle|\; \begin{array}{l} \dot{\gamma}\dot{\beta}_1 \geq 0; \quad \dot{\gamma}\dot{\beta}_3 \leq 0; \quad \text{if} \quad \gamma > 0 \\ \dot{\gamma}\dot{\beta}_2 \leq 0; \quad \dot{\gamma}\dot{\beta}_3 \geq 0; \quad \text{if} \quad \gamma < 0 \end{array} \right\} \tag{3.7}$$

With this new J_χ, it is now necessary to define a correction factor Δx_χ^n for $\partial_i J_\chi$ for Eq. 3.8. Here, the bars have been removed to indicate that the left hand side of Eq. 3.8 is final, accounting for Euler's method and both indicator functions.

$$x_B^{n+1} = \overline{\overline{x}}_B^{n+1} + \Delta x_\chi^n \tag{3.8}$$

Figure 3.3 offers a pictorial representation of the indicator function law. In these plots, the gray shaded areas represent when J_χ is obeyed. In the unshaded areas where J_χ has been violated, the arrows represent a correction where either $\dot{\beta}_i$ or $\dot{\gamma}$ is set to zero. Lastly, the dotted lines split the quadrants where violations occur and determine which of the aforementioned corrections take place. Note that since a correction sets the time derivative to zero, the equivalent numerical correction is to set the value of the martensite fraction equal to its value from the previous time step.

A numerical summary of Fig. 3.3 is shown below in Table 3.3.

Table 3.3: Constraint Law for J_χ

$\gamma > 0$		$\gamma < 0$	
$\dot{\gamma}\dot{\beta}_1 < 0$	$\dot{\gamma}\dot{\beta}_3 > 0$	$\dot{\gamma}\dot{\beta}_2 > 0$	$\dot{\gamma}\dot{\beta}_3 < 0$
$\lvert\dot{\gamma}\rvert \geq \lvert\dot{\beta}_1\rvert$	$\lvert\dot{\gamma}\rvert \geq \lvert\dot{\beta}_3\rvert$	$\lvert\dot{\gamma}\rvert \geq \lvert\dot{\beta}_2\rvert$	$\lvert\dot{\gamma}\rvert \geq \lvert\dot{\beta}_3\rvert$
$\Delta\beta_1 = x_{B,1}^n - \overline{\overline{x}}_{B,1}^{n+1}$	$\Delta\beta_3 = x_{B,3}^n - \overline{\overline{x}}_{B,3}^{n+1}$	$\Delta\beta_2 = x_{B,2}^n - \overline{\overline{x}}_{B,2}^{n+1}$	$\Delta\beta_3 = x_{B,3}^n - \overline{\overline{x}}_{B,3}^{n+1}$

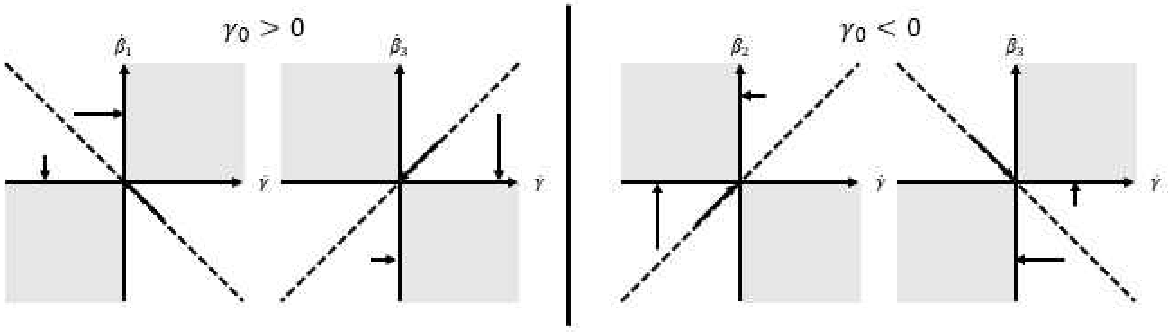

Figure 3.3: Constraint law for J_χ

Compiling Martensite Fractions

An interesting issue that arises with the differential equations in Eq. 2.19, Eq. 2.20, and Eq. 2.21 is that the shear stress is a function of the radial coordinate r. Therefore, the martensite fractions should, in theory, have a different value at every radius. Since it is assumed that the martensite fractions are constant throughout the entire cross-section in the homogeneous case and constant past the critical radius in the bilinear case, the assumption that a different value of β_i at every r cannot hold. This issue is circumvented by obtaining an average martensite fraction. This average martensite fraction is calculated by considering a weight function, like the one in Eq. 3.9. Note that the equation is not unlike finding the centroid of an arbitrary area.

$$\beta_{i,avg} = \frac{\int_A \beta_i dA}{\int_A dA} \tag{3.9}$$

Equation 3.9 can be simplified. The first step is to construct a vector of radius values from the center to the edge of the SMA wire, $r = [0 : \Delta r : d/2]$, where Δr is the step size between radius values. Focusing on the differential area dA next, the cross section of the SMA spring is a circle, so $dA = 2\pi r dr$. With the differential area defined, the denominator can be solved, with its solution posted below in Eq. 3.10.

$$\int_A dA = 2\pi \int_{r_T}^{d/2} r dr = \pi \left[\left(\frac{d}{2} \right)^2 - r_T^2 \right] \tag{3.10}$$

The solution of the numerator is only slightly more sophisticated. Since β_i in the integral is finite, the integral must be approximated as a Riemann sum. The integral, therefore, is converted into the summation exhibited in Eq. 3.11.

$$\int_A \beta_i dA = 2\pi \int_{r_T}^{d/2} \beta_i r dr \approx 2\pi dr \sum_{j=j_{r_T}}^{N_r} \beta_{i,j} r_j \tag{3.11}$$

where N_r is the number of elements in the radius vector and j_{r_T} is the index that corresponds to the radial coordinate past r_T in the vector r. Equation 3.12 is the resulting average martensite fraction when the numerator and denominator are combined.

$$\beta_{i,avg} = \frac{2dr \sum_{j=j_{r_T}}^{N_r} \beta_{i,j} r_j}{(d/2)^2 - r_T^2} \tag{3.12}$$

Note that the average martensite fraction is undefined when $r_T = d/2$. When the critical radius is the radius of the SMA wire, however, there should be, in theory, no detwinned martensite phase transformations present. Therefore, as discussed earlier, $\beta_1 = \beta_2 = \beta_4 = 0$ and $\beta_3 = 1$.

Numerical Summary

For clarity of the entire numerical process, Fig. 3.4 offers a flowchart of the steps taken to solve the state variables. Note that the radius "for loop" is contained within the time "for loop". Otherwise, the average martensite fraction at a certain time cannot be calculated, since the martensite fractions at each radius are needed. Also note that the solution of the displacement and velocity comes before the solution of the martensite fractions. The martensite-fractions calculations are second because of the nature of the split operator technique. According to Savi and Braga, the value of the displacement at the next time step u^{n+1} is needed to obtain the values of the martensite fractions at the next time step [28].

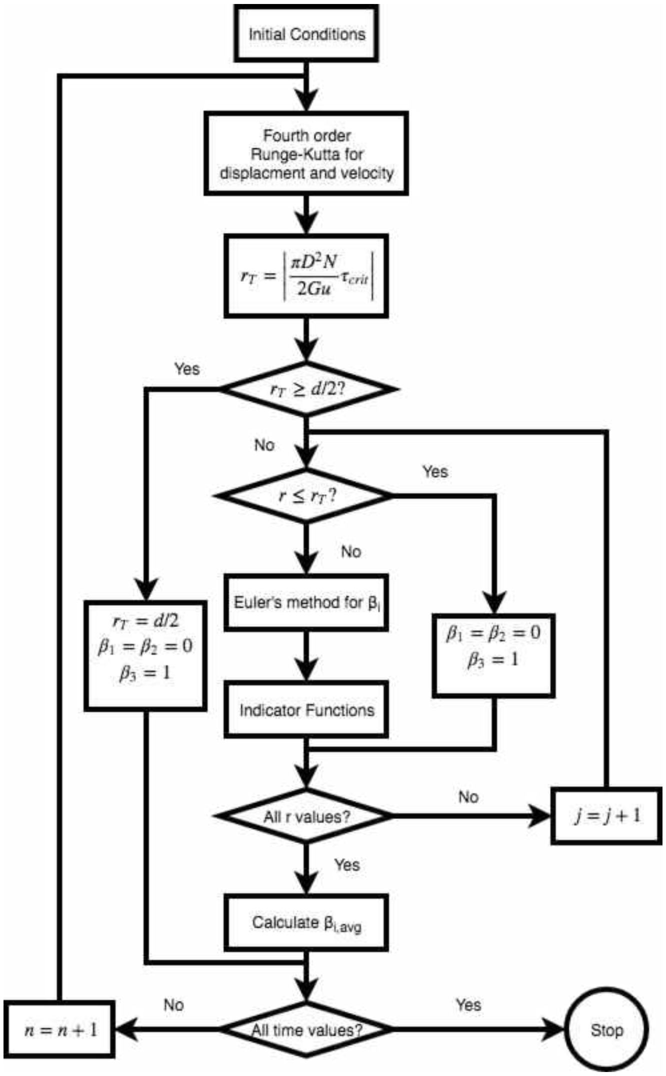

Figure 3.4: Numerical Flowchart

CHAPTER 4: RESULTS AND DISCUSSION

For the following results, it is assumed that the mass of the system from Eq. 1.4 is $m = 2.0\,\mathrm{kg}$, and that there is no external damping, such that $c = 0$. The system will not have any applied forces either (i.e., $f(t) = 0$). Some other parameters that will be kept constant are highlighted in Table 4.1 and Table 4.2. These constant values come from [16], with the exception of the minimum critical normal stress $\sigma_s^{\min}$ and the temperature stress parameter C_M, which are reasonable values partially derived from [1].

Table 4.1: SMA Spring Parameters

D (mm)	d (mm)	N	G_A (GPa)	G_M (GPa)	α (MPa)	γ_R	T_M (K)
6	0.75	20	14.5	11.5	40	0.028	303

The results are organized such that the effects of the initial displacement u_0 are first examined, then the temperature T. Within each section, the plots are presented in the following order: displacement and velocity versus time, phase, martensite fractions versus time, force versus displacement shear stress versus radius and time, and critical radius versus time when applicable. The plots for the homogeneous case are presented first, then the bilinear case.

Table 4.2: SMA Spring Martensite-Fractions Parameters

L_0^M (kPa)	L^M (MPa)	L_0^A (kPa)	L^A (MPa)	$\sigma_s^{\min}$ (MPa)
0.6	29.5	0.03	48.5	100
$\eta_{1,2}^L$ (MPa s)	$\eta_{1,2}^U$ (MPa s)	η_3^L (MPa s)	η_3^U (MPa s)	C_M (MPa/K)
220	20	220	23	8

To determine if one martensite-fractions distribution is better model than the other, there are certain key assumptions that the plots must meet. The first of these assumptions is that the displacement and velocity converge to zero as an equilibrium point. In other spring-mass systems, the system tends to oscillate around zero as an equilibrium point, so it is reasonable to expect the same trend with an SMA-spring. Another assumption is that β_3 must converge to one. Since the spring is initially in the austenite phase when at rest, the spring should also end up in the austenite phase. The third assumption is that the twinned martensite fraction β_4 should equal zero at all times. With the assumption that the temperature is constant throughout the operation of the system, there should be no phase changes as a result of temperature. The fourth assumption is that β_1 should equal zero when β_2 is non-zero and vice versa. Since β_1 and β_2 are detwinned martensite fractions associated with positive and negative stress, respectively, negative and positive stresses cannot occur at the same time. One final assumption is that the force-displacement should resemble the pseudoleastic stress-strain plot. This assumption is seen in the literature [16].

Initial Displacement

For this section, four values were chosen for the initial displacement: $u_0 = 0.05\,\mathrm{m}$, $u_0 = 0.10\,\mathrm{m}$, $u_0 = 0.30\,\mathrm{m}$, and $u_0 = 0.50\,\mathrm{m}$, while the temperature was held constant at $T = 343\,\mathrm{K}$.

The first plots to be examined in this section are the displacement and velocity responses. Figs. 4.1 illustrate the displacement and velocity for the homogeneous assumption. Note that despite the fact that there is no external damper present or friction, decay is nevertheless present in both the displacement and velocity. This observation is promising, since it implies that the decay is the resulting of the changing martensite fractions, which is what should be observed in an SMA spring. For an ideal spring with no external damping or friction, the system would simply be oscillating without decaying for all time. It is interesting to note that the decay does not converge to zero, but instead oscillates at a constant amplitude that is lower than the initial displacement. For all of the initial displacements, this steady state amplitude is aproximately 0.026 m. One last feature of note is that the damping increases with increasing u_0. Using the logarithmic decrement method, the damping ratio when $u_0 = 0.30\,\mathrm{m}$ is $\zeta = 2.43\%$. The other damping ratios are listed below in Table 4.3.

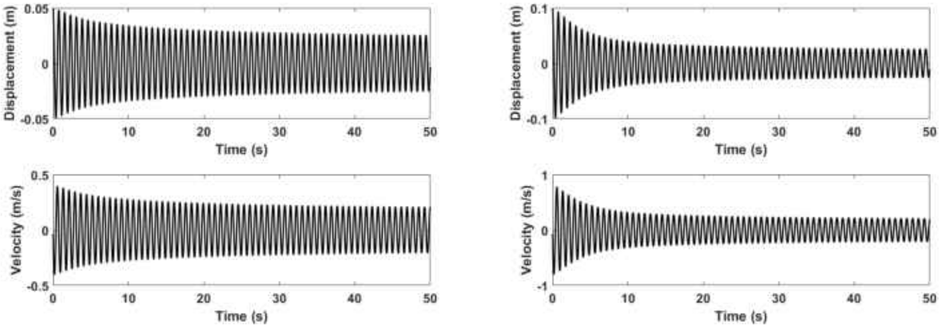

(a) $u_0 = 0.05\,\mathrm{m}$ (b) $u_0 = 0.10\,\mathrm{m}$

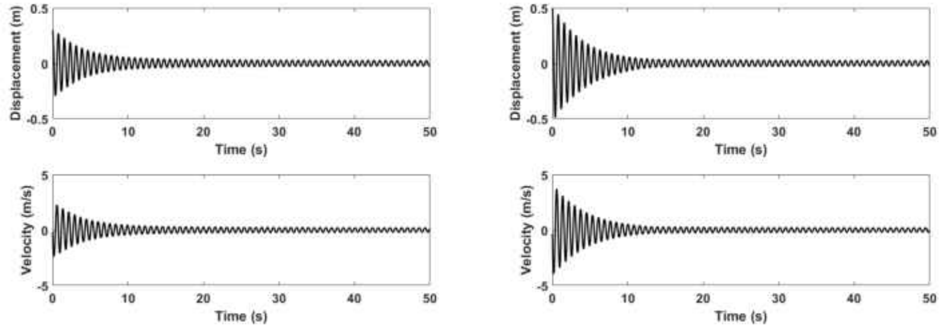

(c) $u_0 = 0.30\,\mathrm{m}$ (d) $u_0 = 0.50\,\mathrm{m}$

Figure 4.1: Homogeneous Position and Velocity Responses for Various Initial Displacements

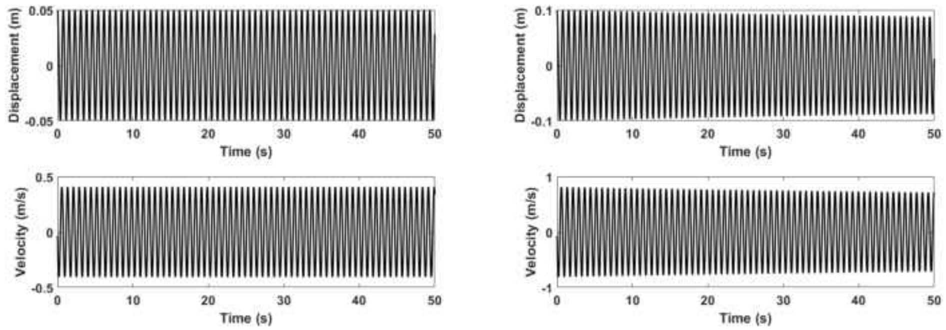

(a) $u_0 = 0.05\,\mathrm{m}$ (b) $u_0 = 0.10\,\mathrm{m}$

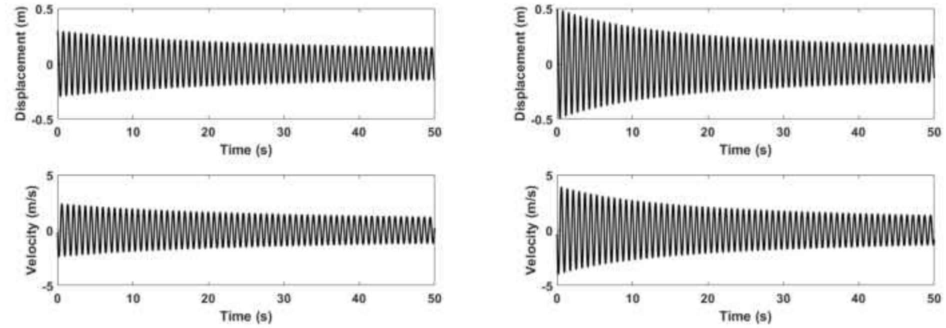

(c) $u_0 = 0.30\,\mathrm{m}$ (d) $u_0 = 0.50\,\mathrm{m}$

Figure 4.2: Bilinear Position and Velocity Responses for Various Initial Displacements

The bilinear assumption shows similar results. Many of the features seen in the homogeneous assumption are also seen in this other assumption. The damping continues to increase with larger initial displacements, and the responses decay down to a steady state sinusoidal response. There is a key difference, however, between the responses of the two assumptions. The decay has been greatly reduced. The largest decay reported in Figs. 4.2 is $\zeta = 0.58\%$, which is smaller than the smallest damping ratio for the homogeneous case. For $u_0 = 0.05\,\mathrm{m}$, there is, in fact, no damping. This result is because the displacement is so small, the critical radius r_T in Eq. 2.29 must always equal the outer radius $d/2$. Therefore, there exists a threshold initial displacement where there is no damping present from the SMA itself, and damping would come from friction and any external dampers. Despite this issue, it is reasonable to assume that there are initial displacements that are too small for hysteretic damping to activate.

Table 4.3: Damping Ratios for Various Initial Displacements

Damping Ratio ζ (%)		
u_0 (m)	Homogeneous	Bilinear
0.05	0.68	0
0.10	1.51	0.04
0.30	2.43	0.30
0.50	2.70	0.58

The features observed the displacement and velocity graphs in Fig. 4.1 are shown in a different light in the phase plots in Figs. 4.3. The increase in damping as u_0 increases is highlighted by the limit cycles being much smaller than the initial displacement and the gaps between the spirals being spaced further apart.

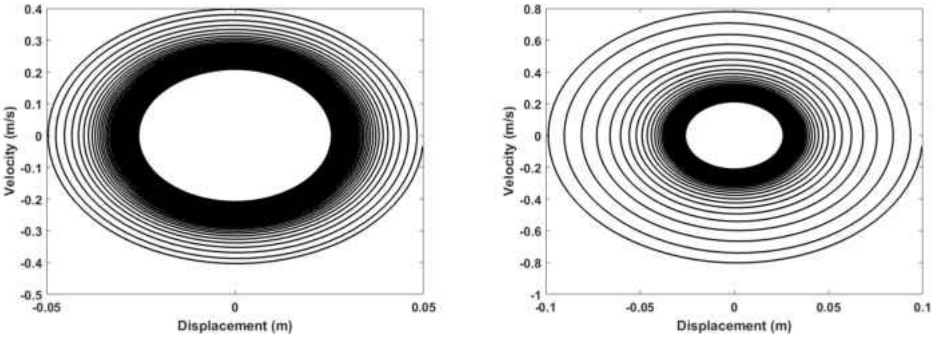

(a) $u_0 = 0.05\,\mathrm{m}$ (b) $u_0 = 0.10\,\mathrm{m}$

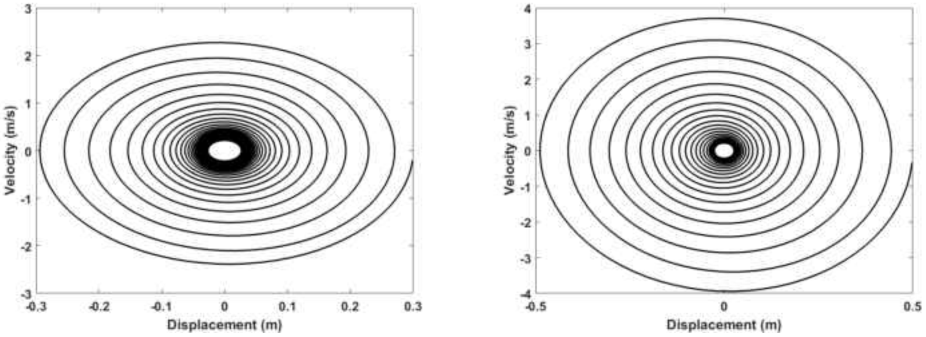

(c) $u_0 = 0.30\,\mathrm{m}$ (d) $u_0 = 0.50\,\mathrm{m}$

Figure 4.3: Homogeneous Phase Plots for Various Initial Displacements

The phase plots for the bilinear case in Figs. 4.4 also show the differences between the bilinear and homogeneous assumptions. The smaller damping ratios are reflected in the spaces between the spirals being much tighter than in the homogeneous case. In fact, for the cases when $u_0 = 0.10\,\mathrm{m}$ and $u_0 = 0.30\,\mathrm{m}$, the spacing seems nonexistent, and the phase plots seem thick instead. The phase plot for the smallest initial displacement does not show any damping, and is a circle instead of a spiral.

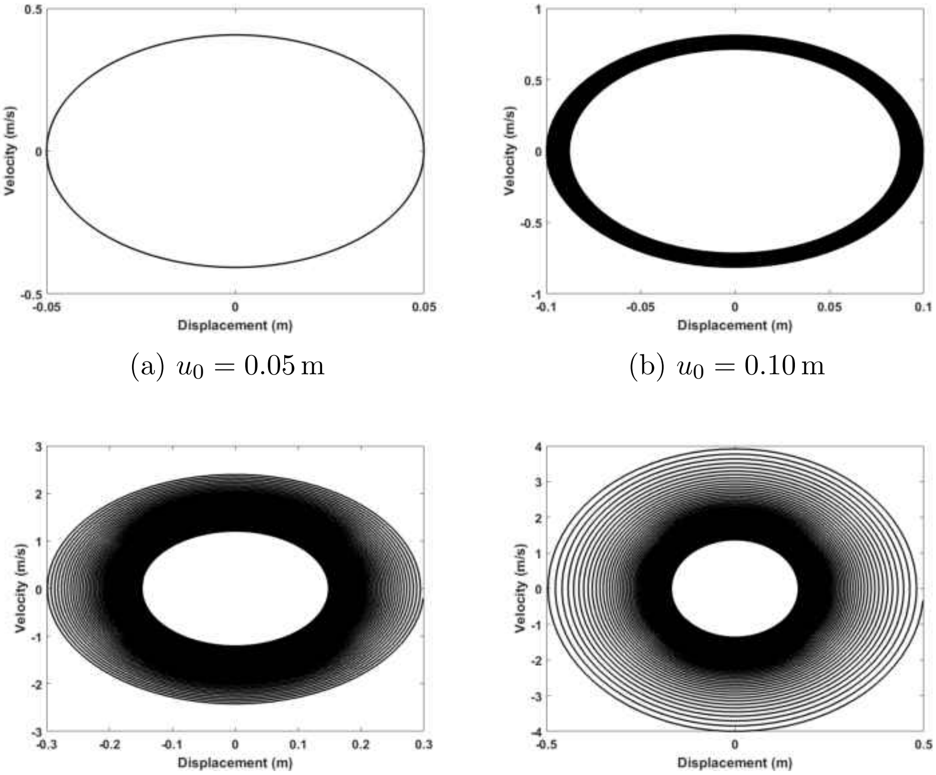

(a) $u_0 = 0.05\,\mathrm{m}$ (b) $u_0 = 0.10\,\mathrm{m}$

(c) $u_0 = 0.30\,\mathrm{m}$ (d) $u_0 = 0.50\,\mathrm{m}$

Figure 4.4: Bilinear Phase Plots for Various Initial Displacements

Figures 4.5 demonstrate the evolution of the martensite fractions over time for the different initial displacements under the homogeneous premise. As expected, the martensite fractions for all time only ever have a value between zero and one, and their sum is always equal to one. At times, the martensite fractions have values outside of the desired range, but these anomalies are negligible in magnitude and can be attributed to numerical errors. This attribute hints that the laws for the indicator functions J_π and J_χ are functioning properly. Another feature of the martensite fraction plots is that the twinned martensite fraction β_4 is always equal to zero. Since the plots conform to the third key assumption, it is reassuring to see that the numerical methods output a solution that naturally sets β_4 to zero. One final characteristic that the martensite-fractions plots display is symmetry. The sum of the detwinned martensite fractions $\beta_1 + \beta_2$ is symmetric to the martensite fraction pertaining to austenite β_3 about the line $\beta = 0.5$. The detwinned martensite fractions "trade off" in their peaks, which conforms to the fourth assumption.

As for the homogeneous martensite-fractions plots themselves, there is a sharp decrease in value for β_3 within the first few seconds of the SMA-spring-mass system's operation. The dip in value for β_3 correlates to an increase in the detwinned martensite fractions. As the initial displacement increases, so does the magnitude of the dip and spike. Eventually, the martensite fractions converge to extreme values, with $\beta_3 = 1$ and $\beta_1 = \beta_2 = \beta_4 = 0$. This steady state behavior suggests that β_3 is the martensite fraction that dominates over the other phase fractions. The behavior for the largest initial displacement deviates from the behavior of the other three values of u_0. The symmetry between β_3 and the detwinned martensite fractions no longer applies, and the fourth key assumption is violated. This result shows a limitation in using the homogeneous distribution for this initial displacement.

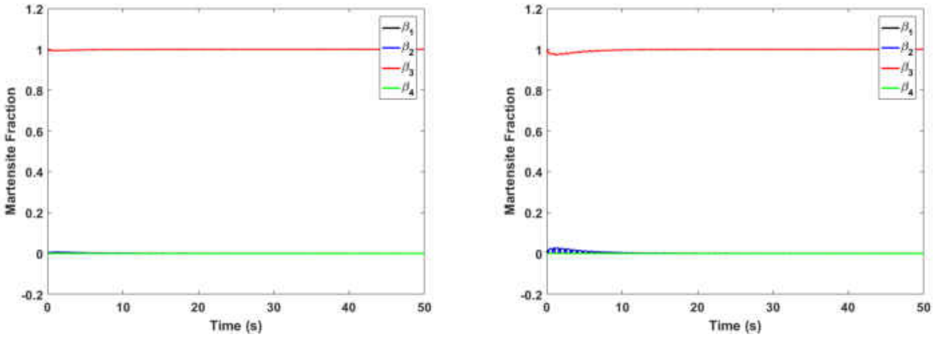

(a) $u_0 = 0.05\,\mathrm{m}$ (b) $u_0 = 0.10\,\mathrm{m}$

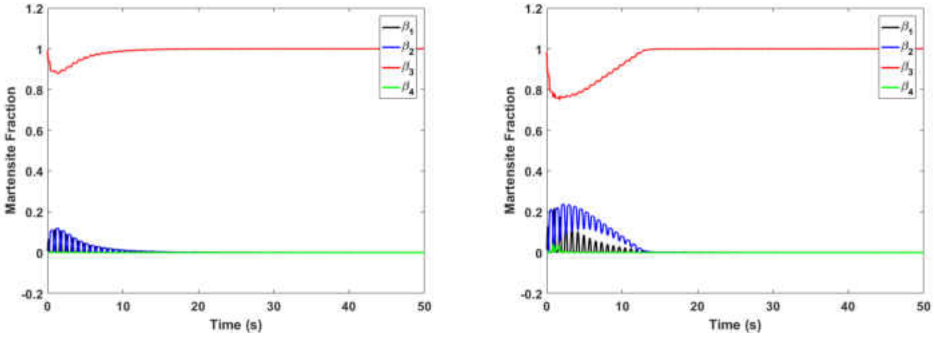

(c) $u_0 = 0.30\,\mathrm{m}$ (d) $u_0 = 0.50\,\mathrm{m}$

Figure 4.5: Homogeneous Martensite-Fractions Plots for Various Initial Displacements

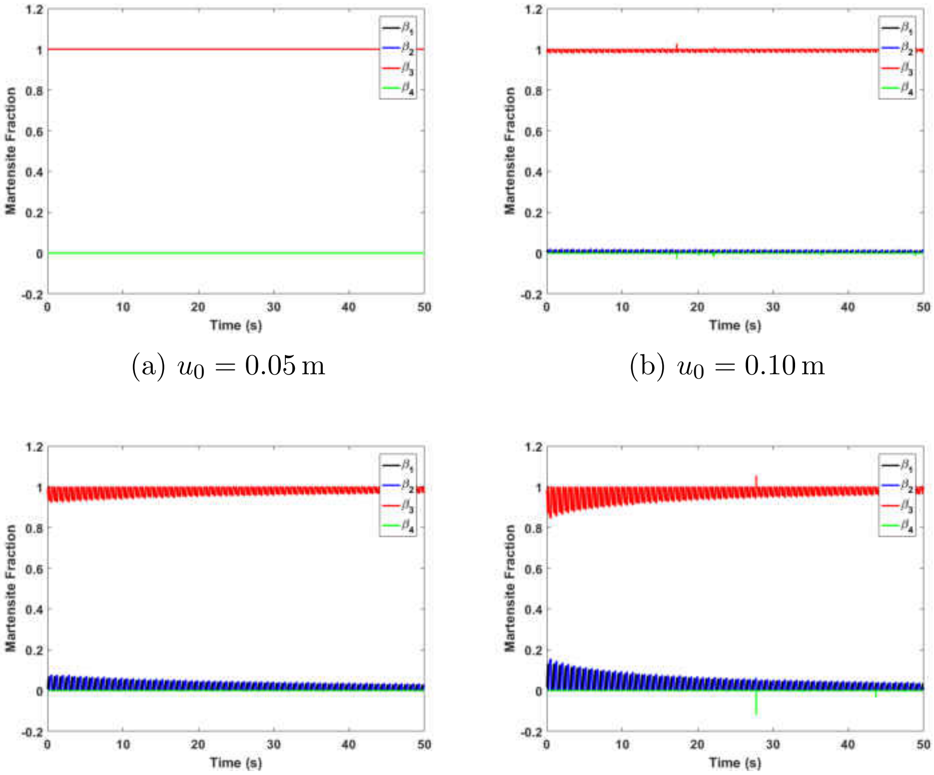

(a) $u_0 = 0.05\,\mathrm{m}$

(b) $u_0 = 0.10\,\mathrm{m}$

(c) $u_0 = 0.30\,\mathrm{m}$

(d) $u_0 = 0.50\,\mathrm{m}$

Figure 4.6: Bilinear Martensite-Fractions Plots for Various Initial Displacements

The martensite-fractions plots for the bilinear case in Figs. 4.6 show drastically different results from their homogeneous counterparts. Like the homogeneous case, these martensite fractions do not violate the laws from Eq. 2.10 and Eq. 2.11 (with the exception of a few spikes that are most likely numerical errors) and still exhibit symmetry between β_3 and the detwinned martensite fractions. The twinned martensite fraction β_4 also equals zero for all time, as expected, and the martensite fractions eventually converge to an extreme value. A major difference between the homogeneous and bilinear cases is that the symmetry between the detwinned martensite fractions and β_3 persists in the bilinear case, and β_1 and β_2 "trade-off" of each other, meeting the fourth assumption. The twinned martensite fraction β_4 also equals zero for all times and all initial displacements. Additionally, the dip and spike seen in Figs. 4.5 has been converted to an exponential growth and decay, respectively. In fact, for much greater initial displacements (e.g., $u_0 = 2.00\,\mathrm{m}$), β_3 can equal zero for certain times, but it will eventually converge back to one (conversely, $\beta_1 + \beta_3$ can at times equal one, but will eventually converge to zero). One last feature shared among the plots is that the martensite-fractions convergence is much slower and less pronounced than in the homogeneous case. Consistent with the response and phase plots from Fig. 4.1a and Fig. 4.3a, respectively, the plot for $u_0 = 0.05\,\mathrm{m}$ in Fig. 4.6a displays only constant values for the martensite fraction. Since no damping is present, there should not be any phase transformations happening within the SMA. One final note on these martensite plots is that these are the values for the phase fractions past the critical radius r_T. For any radius less than the critical radius, the martensite fractions are $\beta_1 = \beta_2 = \beta_4 = 0$ and $\beta_3 = 1$.

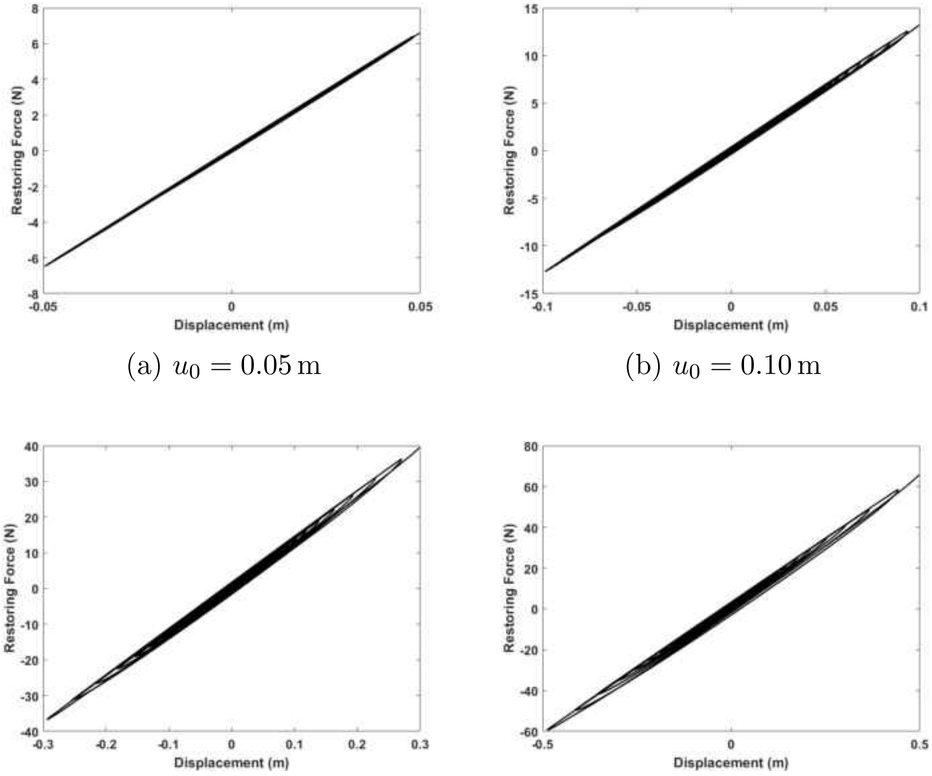

(a) $u_0 = 0.05\,\mathrm{m}$

(b) $u_0 = 0.10\,\mathrm{m}$

(c) $u_0 = 0.30\,\mathrm{m}$

(d) $u_0 = 0.50\,\mathrm{m}$

Figure 4.7: Homogeneous Force Versus Displacement Plots for Various Initial Displacements

The force versus displacement plots in Figs. 4.7 and Figs. 4.8 have a few characteristics in common, despite their differences. One of these traits is that the area of the force-displacement plots expands in size with increasing initial displacement. The increase in size is measured by both the length of the plot and its thickness as well. This growth is seen especially in Fig. 4.7c at the ends, where space between the lines is evident. The other trait is that the plots show rotational symmetry about the origin. Moving onto the homogeneous assumption, the main factor is that force-displacement plots resemble something akin to viscoelastic damping, which does not match the fifth key assumption.

The bilinear force-displacement charts display some intriguing results. There is a change in the behavior for $u_0 = 0.05\,\mathrm{m}$ in Fig. 4.8a. The line has no thickness, which suggests that there is no damping. This result is consistent with what was seen in the other plots so far. There is also less damping for all the plots as well, which is also in agreement with the other plots in the bilinear assumption. Perhaps the most interesting feature of the force-displacement plots is that the plot resembles the pseudoelastic stress-strain diagram from Fig. 1.3, which corresponds to the final key assumption. The pseudoelastic effect is also seen in the third quadrant of the plots in Figs. 4.8, which shows that the pseudoelastic effect takes place for negative displacements as well. The appearance of the pseudoelastic effect suggests that the bilinear case, when compared to the homogeneous assumption, is a more accurate model that better captures the truth of what happens within an SMA spring.

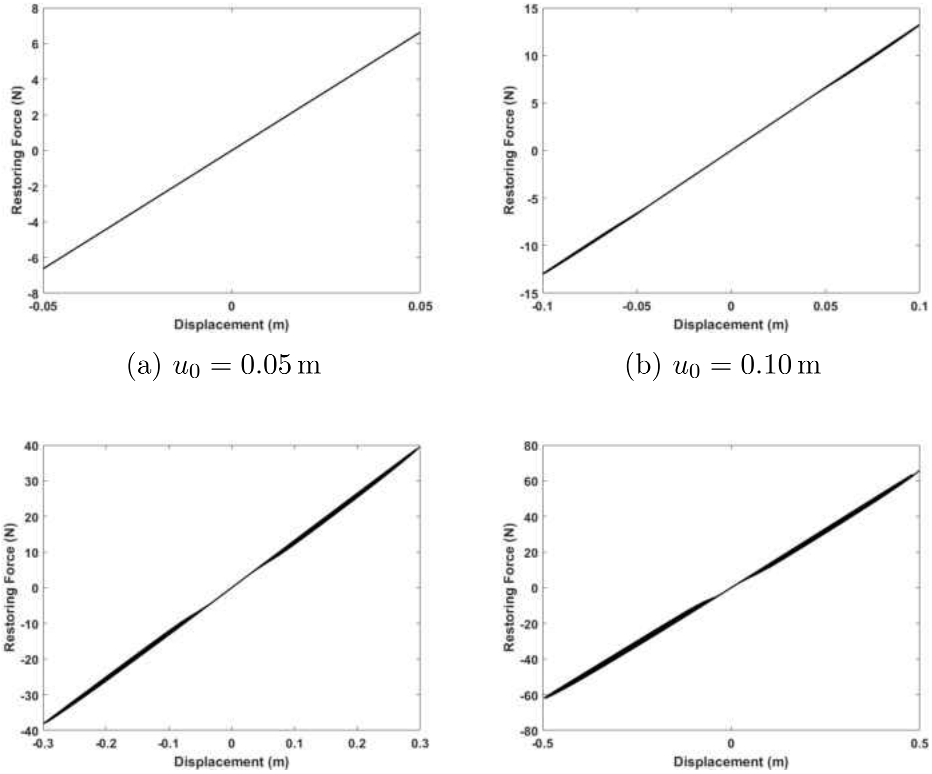

(a) $u_0 = 0.05\,\mathrm{m}$

(b) $u_0 = 0.10\,\mathrm{m}$

(c) $u_0 = 0.30\,\mathrm{m}$

(d) $u_0 = 0.50\,\mathrm{m}$

Figure 4.8: Bilinear Force Versus Displacement Plots for Various Initial Displacements

Another set of plots presents the shear stress τ, which from Eq. 2.28, is a function of the radius r and time t (the radius is presented nondimensionally as $\delta = 2r/d$ for clarification). For both the homogeneous and bilinear cases, the effect of time on the shear stress is that the shear stress decays and oscillates over time, until it reaches a steady state oscillation. In fact, when considering the effect of time alone, the shear stress resembles the displacement. This result is not surprising, since the shear strain γ in Eq. 2.28 is directly proportional to the displacement. As for the radius, the shear stress grows as the radius increases in value. This result also makes sense. With the restoring force creating a torque on the SMA wire, the resulting shear stress should increase for radii further away from the center, which is what is observed. One last shared feature is that the shear stresses are quite large. For the largest initial displacements, the shear strain is approximately 16%. Focusing now on the homogeneous case portrayed in Figs. 4.9, the slope of the shear stress with respect to the radius is constant, though the value of this constant varies with time. This development is expected under the homogeneous approach. In a traditional material, the shear stress under torsion increases linearly across the cross-section. The presence of the extra term $\alpha\left(\beta_2 - \beta_1\right)$ in Eq. 2.28 will not change the slope at a particular time step.

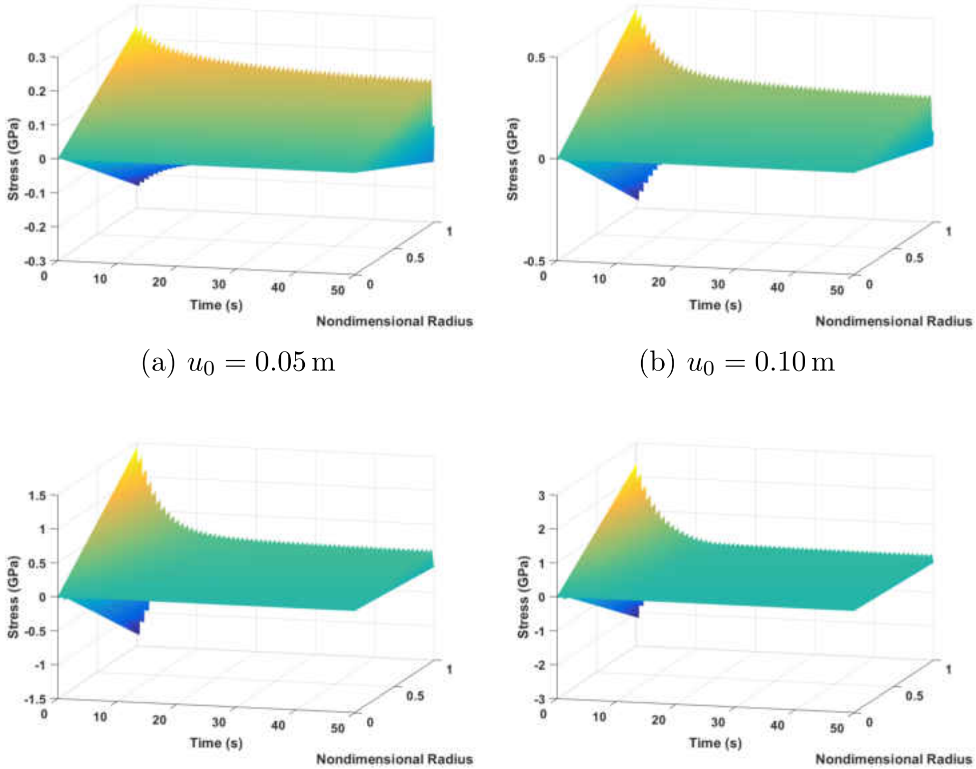

(a) $u_0 = 0.05\,\mathrm{m}$ (b) $u_0 = 0.10\,\mathrm{m}$

(c) $u_0 = 0.30\,\mathrm{m}$ (d) $u_0 = 0.50\,\mathrm{m}$

Figure 4.9: Homogeneous Shear Stress Plots for Various Initial Displacements

The bilinear shear stress graphs in Figs. 4.10 follow the same trends as their homogeneous counterparts. Since the damping for the bilinear displacement response is less than the damping for the homogeneous case, the shear stress also decays less rapidly in the bilinear case. The shear stress also increases linearly as the radius gets larger. One key difference between the homogeneous and bilinear assumptions is that there are two constant slope regimes: one between $0 \leq r \leq r_T$ and the other past the critical radius. The value of the slope before the critical radius is always greater in value than the slope past r_T. This result is to be expected as well. Since the martensite fractions are constant past the critical radius, the shear stress should increase linearly past the critical radius as well, and since the slope is at a maximum within the critical radius (since $G = G_A$ because $\beta_3 = 1$), the slope of the shear stress with respect to the radius beyond the critical radius can only ever be less than the maximum slope.

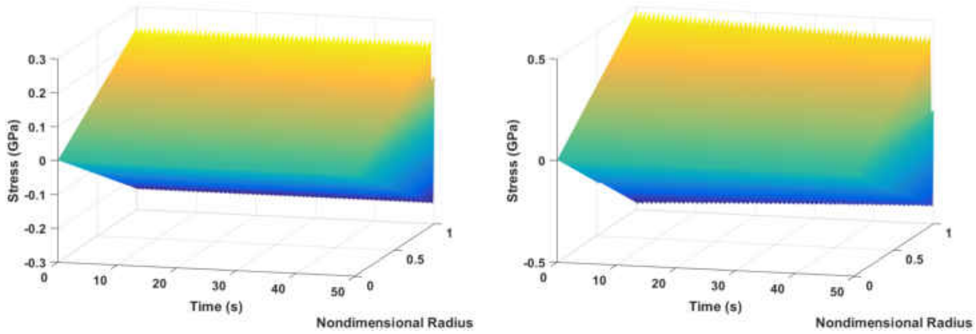

(a) $u_0 = 0.05\,\mathrm{m}$ (b) $u_0 = 0.10\,\mathrm{m}$

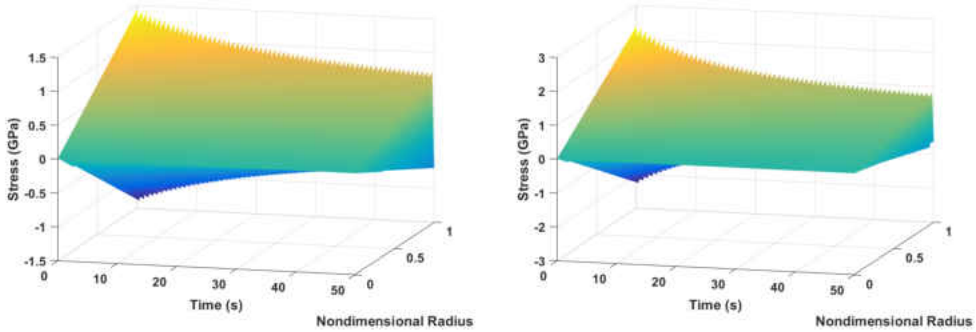

(c) $u_0 = 0.30\,\mathrm{m}$ (d) $u_0 = 0.50\,\mathrm{m}$

Figure 4.10: Bilinear Shear Stress Plots for Various Initial Displacements

The last set of plots to examine are those of the critical radius as a function time, shown in Figs. 4.11, as the plots bring to light the phenomena observed in the bilinear graphs (again, the critical radius is nondimensionalized to $\delta_T = 2r_T/d$ for clarification). For the case where $u_0 = 0.05\,\mathrm{m}$ in Fig. 4.11a, the initial displacement is too small for the critical radius to ever have a value lower than $d/2$. Thus, the SMA-spring-mass system never decays, the martensite phase fractions remain constant, and the force-displacement graph is an ideal straight line with no thickness. As for the other initial displacements, the critical radius seems to oscillate between the nondimensional upper limit of $\delta_T = 1$ and a lower limit that increases in value over time. When $u_0 = 0.10\,\mathrm{m}$, the lower critical radius gives relatively large values. When $u_0 = 0.30\,\mathrm{m}$ and $u_0 = 0.50\,\mathrm{m}$, both critical radius plots converge to a steady state value of $\delta_T \approx 0.25$, but Fig. 4.11d does so much more quickly than Fig. 4.11c. From a mathematical standpoint, the system's amplitude decays (so that the lower limit increases) until it eventually reaches a limit cycle whose amplitude, despite being as small as possible, is still too large for the critical radius to equal the outside radius of the SMA wire (and therefore converges). Also the quicker convergence for larger initial displacements is in step with the larger damping for larger values of u_0.

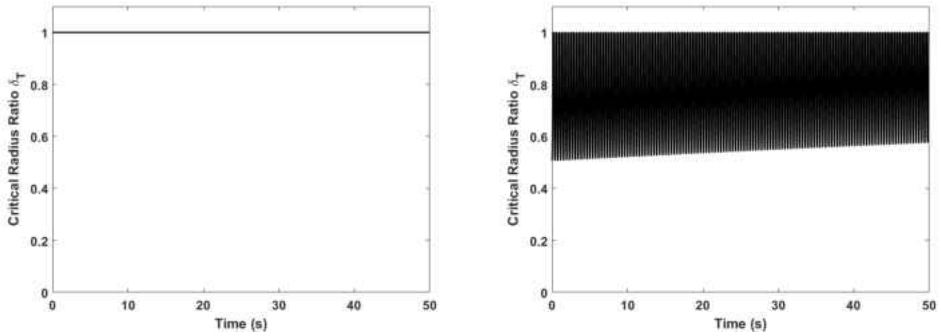

(a) $u_0 = 0.05\,\mathrm{m}$ (b) $u_0 = 0.10\,\mathrm{m}$

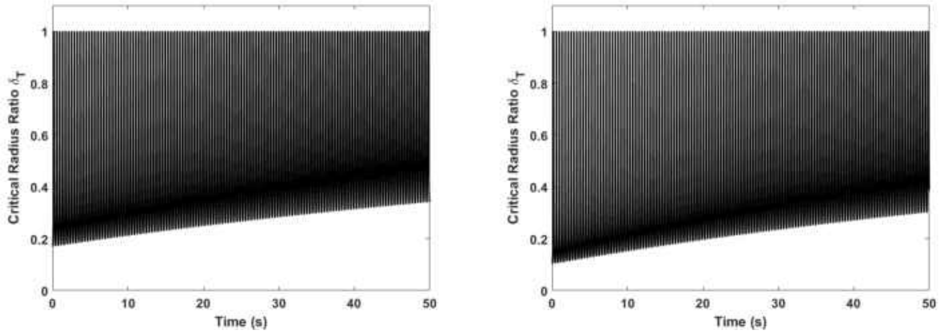

(c) $u_0 = 0.30\,\mathrm{m}$ (d) $u_0 = 0.50\,\mathrm{m}$

Figure 4.11: Critical Radius Plots for Various Initial Displacements

Temperature

This time, the initial displacement was held constant at $u_0 = 0.30\,\mathrm{m}$, and the temperature changes in value. The four temperature values are $T = 298\,\mathrm{K}$, $T = 303\,\mathrm{K}$, $T = 343\,\mathrm{K}$, and $T = 403\,\mathrm{K}$. Unlike the initial displacements, the choice of these temperatures is not arbitrary. Since the martensite start temperature is $T_M = 303\,\mathrm{K}$ per Table 4.1, the four values were chosen such that comparisons were made for $T < T_M$, $T = T_M$, $T > T_M$, and $T \gg T_M$.

The first plots to be examined are those that highlight the effect of the temperature on the displacement and velocity. Some general observations on these plots are that the limit cycle amplitudes increase with size as the temperature increases. As a result, the damping decreases as the temperature rises. This observation may be a result of the martensite-fractions differential equations, where Λ_i in Eq. 2.17 is temperature dependent. The increase in the amplitude may also be because of a change in the critical shear stress, which is also a function of the temperature.

The homogeneous plots in Figs. 4.12 follow the trend of larger steady state amplitudes with increasing temperature. One interesting observation is that the steady state amplitude is actually smallest when $T = T_M$ in Fig. 4.12b, suggesting that the case when the operating temperature is the martensite start temperature is a minimum, and the steady state amplitude only increases above or below this minimum.

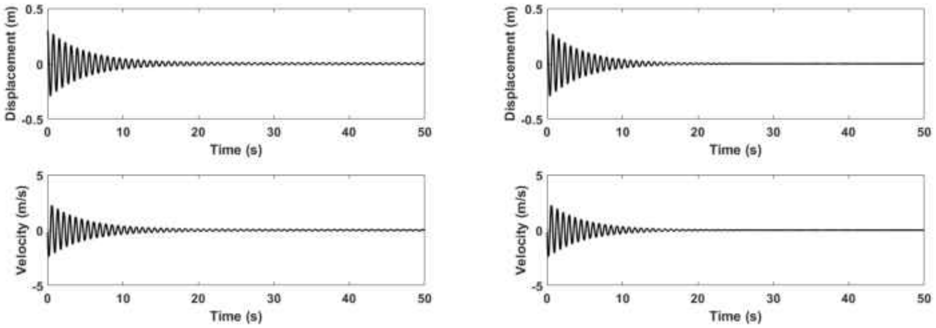

(a) $T = 298\,\mathrm{K}$ (b) $T = 303\,\mathrm{K}$

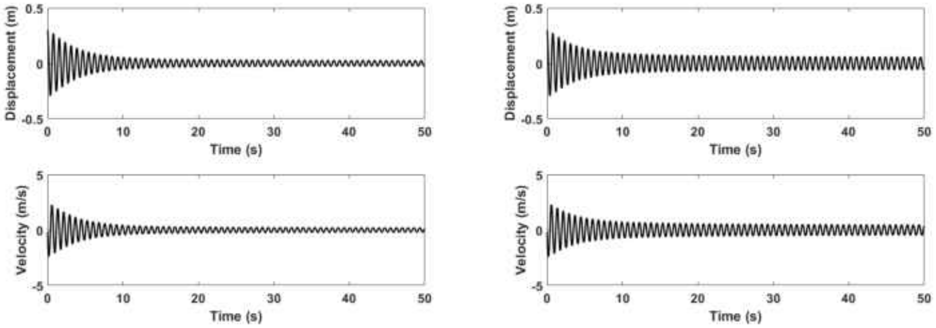

(c) $T = 343\,\mathrm{K}$ (d) $T = 403\,\mathrm{K}$

Figure 4.12: Homogeneous Position and Velocity Responses for Various Temperatures

The bilinear graphs in Figs. 4.13 show some slightly different results. As was seen in Figs. 4.2, the damping is much smaller than in the homogeneous for all temperatures. One key difference is that the minimum detected in the homogeneous plots instead becomes a threshold in the bilinear case. When the temperature is both $T = 298\,\mathrm{K}$ and $T = 303\,\mathrm{K}$, the steady state amplitude is $u_{ss} \approx 0.08\,\mathrm{m}$. The resulting conclusion is a reasonable one. The critical normal stress in Eq. 1.2 is a function of the temperature, but for values past the martensite start temperature $T < T_M$, the critical stress is a constant value $\sigma_s^{\min}$, as seen in Fig. 1.4. For temperatures lower than T_M, the critical stress can never be lower than the minimum critical stress. For the bilinear case, the increase in the steady state amplitude with larger temperatures can be explained by the critical radius being a function of the critical shear stress, which is itself a function of the temperature as mentioned earlier. By increasing the temperature, the critical radius (assuming all other values in Eq. 3.4 are held constant) will also grow in size. Since the critical radius has an upper limit of $d/2$, there is less room left for growth of the critical radius when the set temperature is larger.

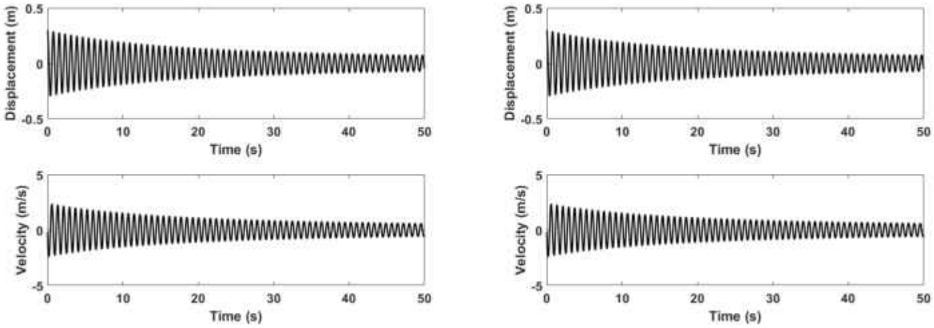

(a) $T = 298\,\mathrm{K}$ (b) $T = 303\,\mathrm{K}$

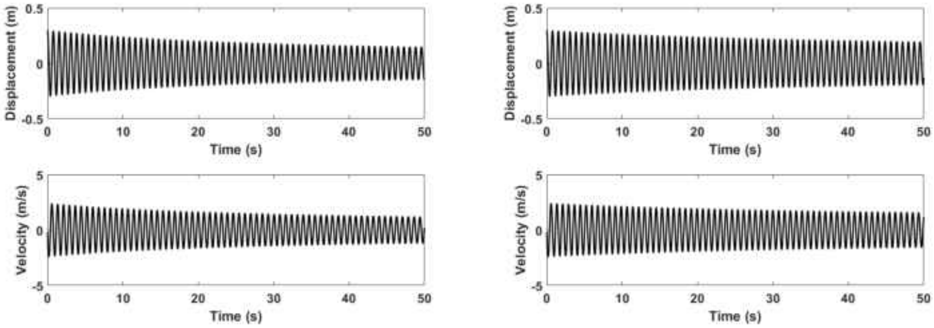

(c) $T = 343\,\mathrm{K}$ (d) $T = 403\,\mathrm{K}$

Figure 4.13: Bilinear Position and Velocity Responses for Various Temperatures

The next set of plots are the phase plots. As with the displacement and velocity plots, the phase plots exhibit larger limit cycles as the temperature rises. Since phase plots are a natural construction of the displacement and velocity as a function of time, which also show this trend, these results are expected. Figures 4.14 illustrate the phase plots for changing temeperature for the homogeneous case. As mentioned earlier, the steady state amplitude for the homogeneous case is smallest when $T = T_M$. This observation from Fig. 4.14b is reflected by the lack of a visible hole within the center of the phase graph, suggesting that the limit cycle is so small, that it cannot be seen.

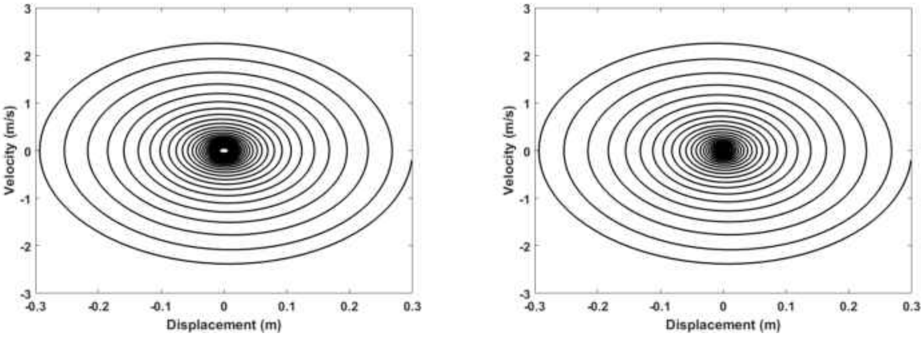

(a) $T = 298\,\mathrm{K}$ (b) $T = 303\,\mathrm{K}$

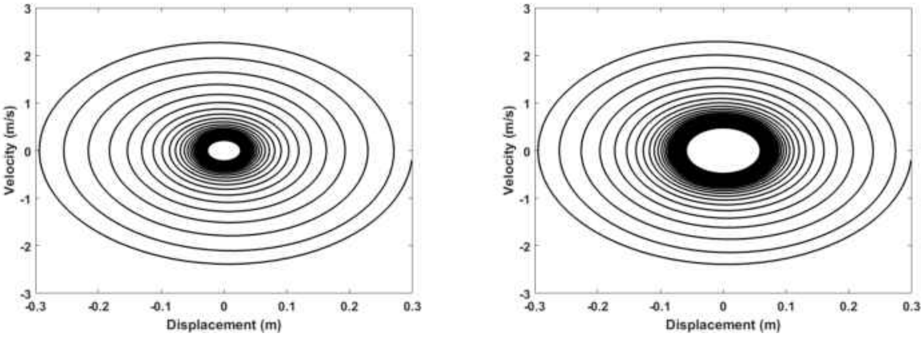

(c) $T = 343\,\mathrm{K}$ (d) $T = 403\,\mathrm{K}$

Figure 4.14: Homogeneous Phase Plots for Various Temperatures

The bilinear phase response in Figs. 4.15 also reflects the observations identified in the displacement and velocity responses. The limit cycle holes in Fig. 4.15a and Fig. 4.15b when $T = 298\,\mathrm{K}$ and $T = 303\,\mathrm{K}$, respectively, are approximately the same size. And as expected, the limit cycle grows in size when the temperature increases. What is interesting to see is just how little damping occurs for the highest temperature $T = 403\,\mathrm{K}$ in Fig. 4.15d, with a limit cycle that does not deviate much from the first spiral. Again, the critical radius and the terms Λ_i are responsible for the the observed trends, as well as the change in results between homogeneous and bilinear assumptions.

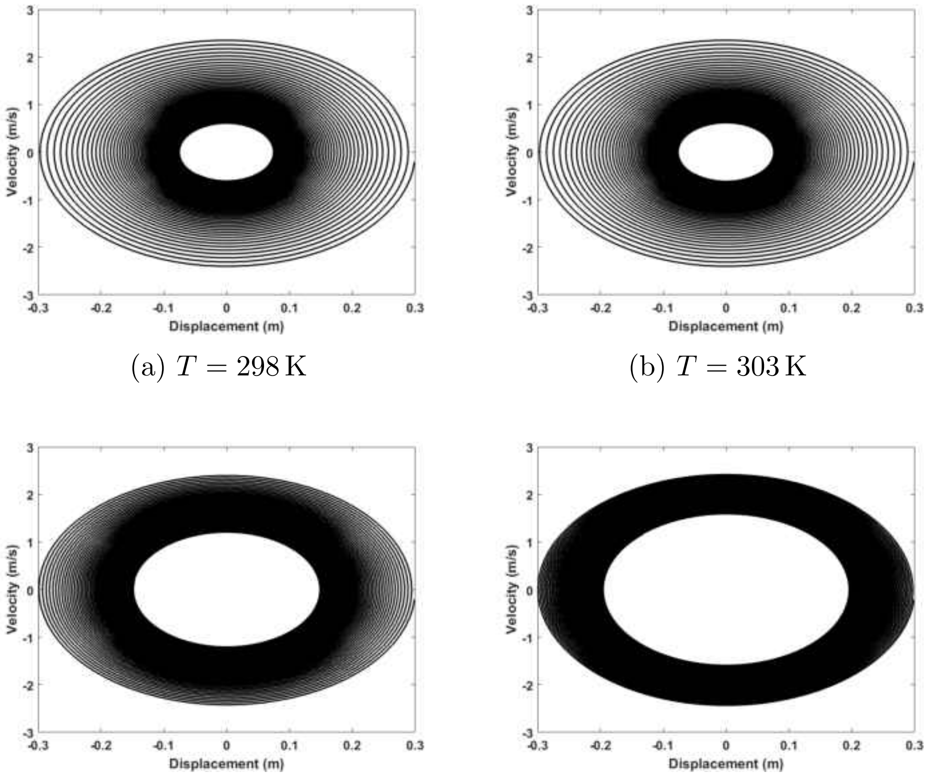

(a) $T = 298\,\mathrm{K}$ (b) $T = 303\,\mathrm{K}$

(c) $T = 343\,\mathrm{K}$ (d) $T = 403\,\mathrm{K}$

Figure 4.15: Bilinear Phase Plots for Various Temperatures

Perhaps the most interesting plots to examine are the martensite fractions as a function of time, since the homogeneous plots are wildly different from the homogeneous plots seen when the initial displacement u_0 varied. As expected, the martensite fractions still follow the laws from Eq. 2.10 and Eq. 2.11. In the homogeneous case in Fig. 4.16, for the instances when $T = 343\,\mathrm{K}$ and $T = 403\,\mathrm{K}$, the martensite phase fraction plots are similar to Figs. 4.5, where there is symmetry between β_3 and $\beta_1 + \beta_2$, and $\beta_4 = 0$ at all times. In fact, Fig. 4.14c and Fig. 4.14d appear to be very similar to one another, which implies that there is some temperature T where the evolution of the martensite fractions remains the same past that temperature. The plots when $T = T_M = 303\,\mathrm{K}$ and $T = 298\,\mathrm{K} < T_M$, however, are quite strange. The third key assumption, that the twinned martensite equal zero at all times, is violated. When $T = T_M$, β_4 rises to a maximum value, then drops for the remainder of the SMA-spring-mass system duration. When $T < T_M$, β_4 continues to rise without ever decreasing in value, while β_3 tends to converge to zero.

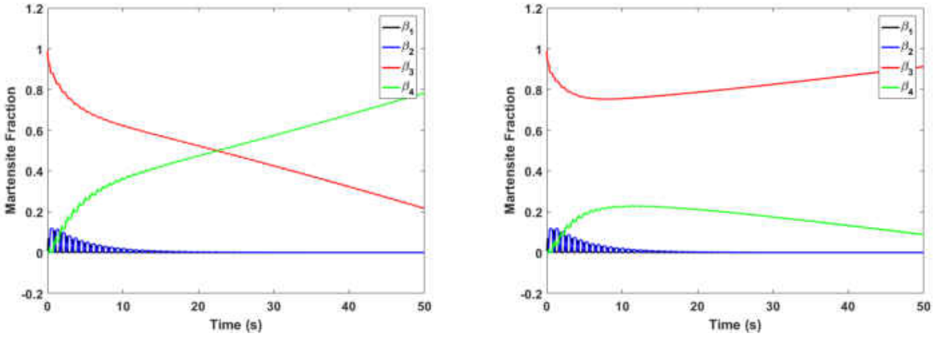

(a) $T = 298\,\mathrm{K}$

(b) $T = 303\,\mathrm{K}$

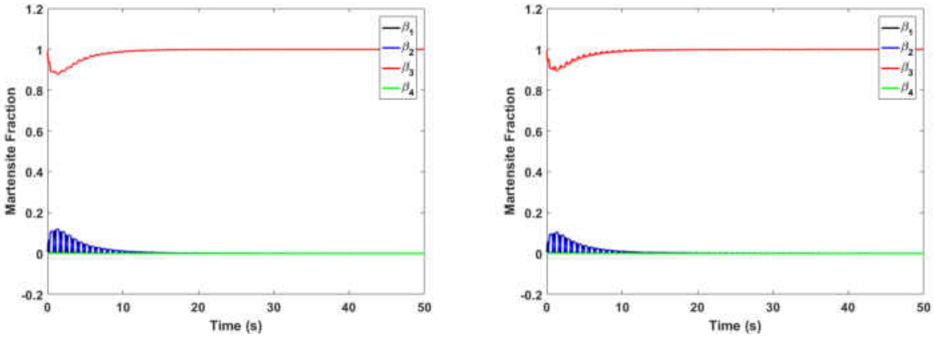

(c) $T = 343\,\mathrm{K}$

(d) $T = 403\,\mathrm{K}$

Figure 4.16: Homogeneous Martensite-Fractions Plots for Various Temperatures

The phase fraction figures for the bilinear case offer results whose phase transformations vary much less than the homogeneous case. As desired, the twinned martensite fraction remains at zero for all time and at all temperatures, which matches the third key assumption. In general, the bilinear plots in Figs. 4.17 greatly resemble the bilinear plots when u_0 varied in Figs. 4.6. This similarity between the plots indicates that the bilinear assumption may be a good fit for the SMA-spring-mass system. When observing the general characteristics, an increase in temperature corresponds to a decrease in the decay and growth of $\beta_1 + \beta_2$ and β_3, respectively, an observation in accordance to the decreased damping as the temperature rose. This response is in opposition to what was seen when the initial displacement was varied, where the decay or growth was directly proportional to the increase in u_0. Also, the growth or decay as the martensite fractions converge is much more subtle than when u_0 varied. These results suggest that changes in the initial displacement affect the system dynamics more than changes in temperature.

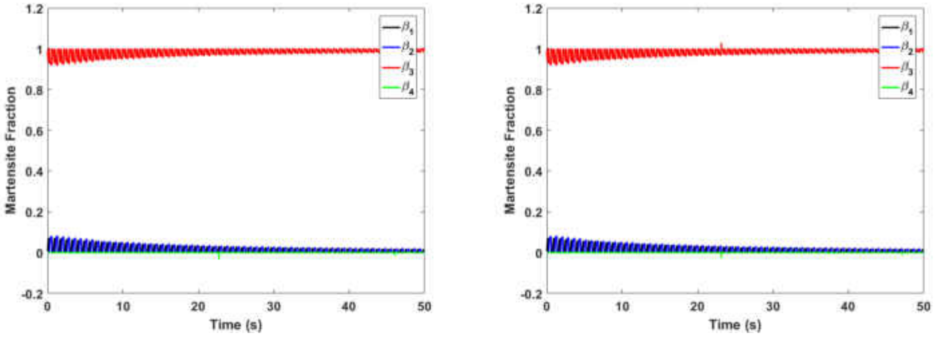

(a) $T = 298\,\mathrm{K}$ (b) $T = 303\,\mathrm{K}$

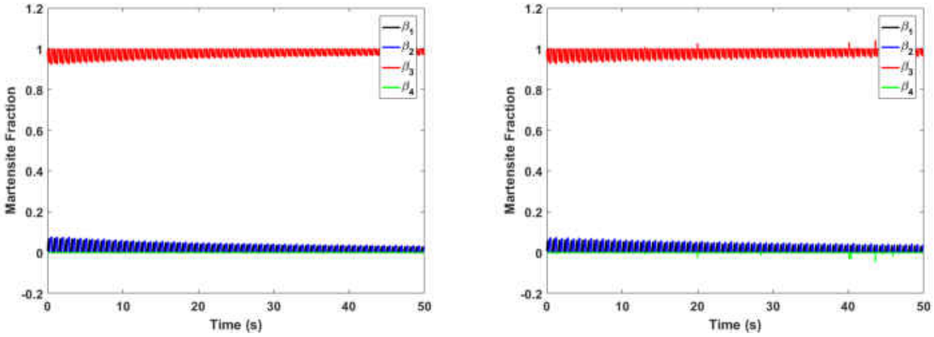

(c) $T = 343\,\mathrm{K}$ (d) $T = 403\,\mathrm{K}$

Figure 4.17: Bilinear Martensite-Fractions Plots for Various Temperatures

The force displacement plots for varying temperatures, both under the homogeneous and bilinear approaches, parallel their counterparts when the initial displacement varies. The force-displacement plots generally follow a straight line that passes through and is symmetric around the origin. Examining the homogeneous plots in Fig. 4.18, the plots do not change much with temperature. The greatest change seen in these plots is that the damping decreases as the temperature rises, as was confirmed in the displacement & velocity plots and phase plots. This decrease in damping is confirmed by the loops in the force-displacement plots getting tighter. The thickness of the loops in Fig. 4.18d is slightly thinner than the loops in Fig. 4.18a.

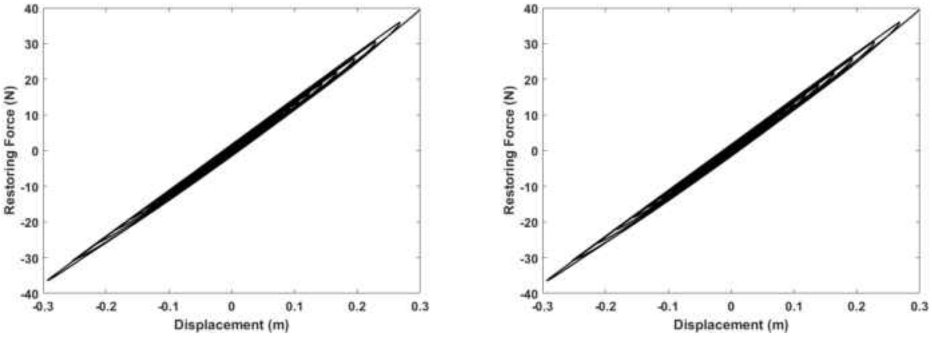

(a) $T = 298\,\mathrm{K}$ (b) $T = 303\,\mathrm{K}$

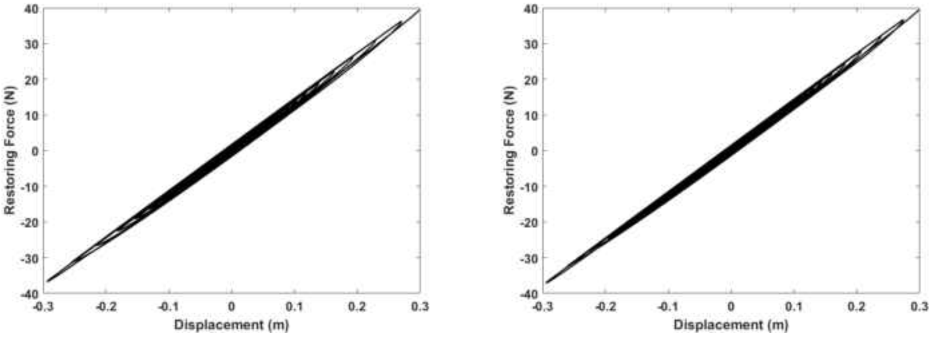

(c) $T = 343\,\mathrm{K}$ (d) $T = 403\,\mathrm{K}$

Figure 4.18: Homogeneous Force Versus Displacement Plots for Various Temperatures

On the other hand, the bilinear plots in Figs. 4.19 are much more intriguing than their homogeneous complements. Like with Figs. 4.8, the force-displacement plots mimic the stress-strain pseudoelastic effect plot in Fig. 1.3, both for positive and negative displacements. When the temperature rises, the damping is reduced, which is seen by two characteristics. The first of these traits is that the thickness of the nonlinear portion of the force-displacement plots gets thinner with increasing temperature. The other trait is that the length of the nonlinear portion also diminishes as the temperature increases. These tendencies are seen as extremes for the force-displacement plots when $T = 298\,\mathrm{K}$ and $T = 403\,\mathrm{K}$. The nonlinear portion of Fig. 4.19a is rather thick, and the ideal elastic portion is short. To the contrary,

Fig. 4.19d has a thinner nonlinear portion, and the elastic portion of the plot is longer than in the other figures. One last observation is that the graphs when $T = 298\,\mathrm{K}$ and $T = 303\,\mathrm{K}$ are near identical (although the hysteretic portions of Fig. 4.19a are somewhat thicker than the sections in Fig. 4.19b). The reduction in size of the hysteresis and the uniformity of the plots between the two lowest temperatures is most likely a result of the critical shear stress. For the two lowest temperatures, the critical shear stress is the minimum critical shear stress in both cases, so the critical radius should not be much different in either case. For the larger temperatures, τ^{crit} increases as the temperature increases, and the critical radius is consequently larger if all other variables in Eq. 3.4 were kept the same. Since r_T is a fundamental part of the force (and can only vary between zero and $d/2$), as seen in Eq. 2.31, larger critical radii will result in less damping, which is exactly what has been seen in Figs. 4.19.

The shear stress figures share many characteristics between homogeneous and bilinear cases. One of these attributes is that the shear stress decay is reduced as the temperature increases. Like with the variation in the initial displacement, this phenomenon is the result of the shear stress being directly proportional to the displacement of the SMA-spring-mass system, with the displacement decaying much more slowly for higher temperatures. Another shared feature of these plots is that the slope of the shear stress with respect to the radius r is constant and increases with a rise in temperature. For the homogeneous case demonstrated in Figs. 4.20, the slope with respect to the radius grows slowly. When $T = 298\,\mathrm{K}$ and $T = 303\,\mathrm{K}$, the steady state radius slopes seem almost flat. The change in the slope when $T = 403\,\mathrm{K}$ in Fig. 4.20d is not much greater than the two lowest temperature cases. The gradual slopes may be a result of the critical stress parameters Λ_i affecting the martensite fractions in Eq. 2.28. The temperature's effect on the displacement may also be responsible for the lower slopes.

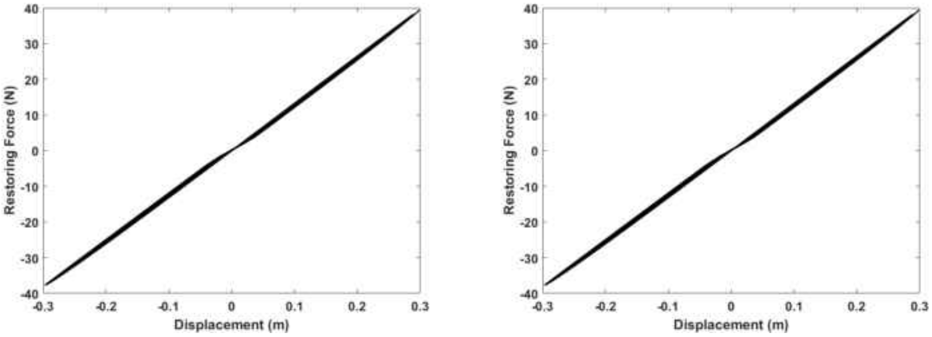

(a) $T = 298\,\mathrm{K}$ (b) $T = 303\,\mathrm{K}$

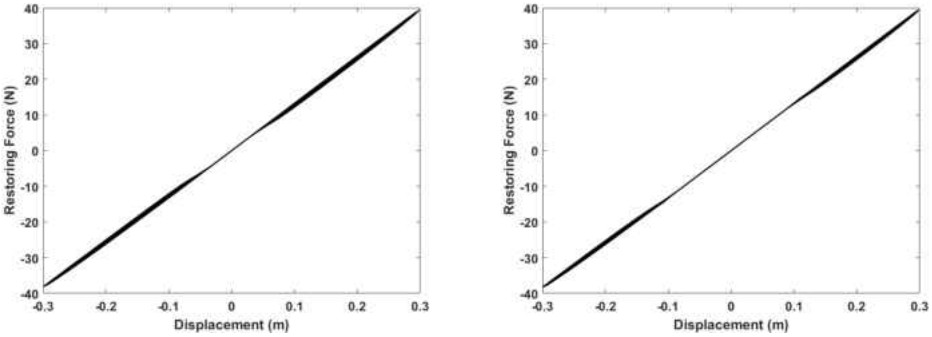

(c) $T = 343\,\mathrm{K}$ (d) $T = 403\,\mathrm{K}$

Figure 4.19: Bilinear Force Versus Displacement Plots for Various Temperatures

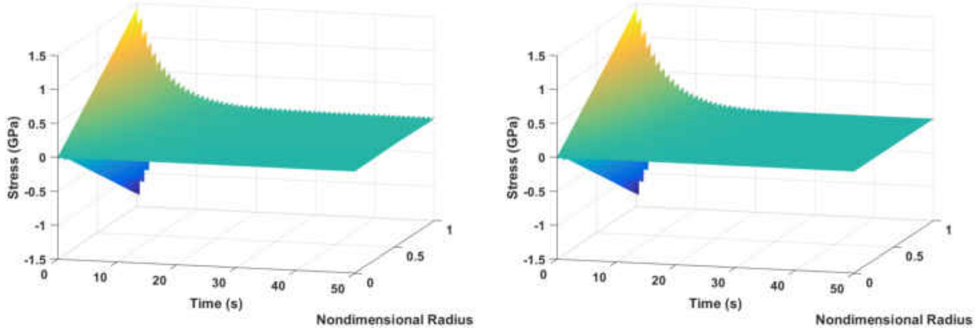

(a) $T = 298\,\mathrm{K}$ (b) $T = 303\,\mathrm{K}$

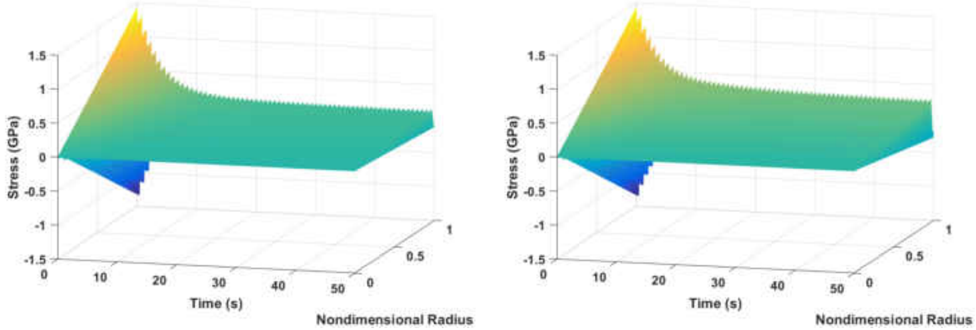

(c) $T = 343\,\mathrm{K}$ (d) $T = 403\,\mathrm{K}$

Figure 4.20: Homogeneous Shear Stress Plots for Various Temperatures

The shear stress plots for the bilinear assumption, displayed in Figs. 4.21, are of course slightly different than their corresponding homogeneous graphs. The slope of the shear stress with respect to the radius is much greater than in the homogeneous case. As with the homogeneous case, this observation can be explained by the displacement and Λ_i. Additionally, the change in the slope decreases with increasing temperature. This is a reasonable result and in accordance with the martensite-fractions plots in Figs. 4.17, since β_3 does not deviate much from its converging value of one, which determines the value of the shear modulus G and therefore determines the slope with respect to the radius (in the term $G\gamma$ in Eq. 2.28).

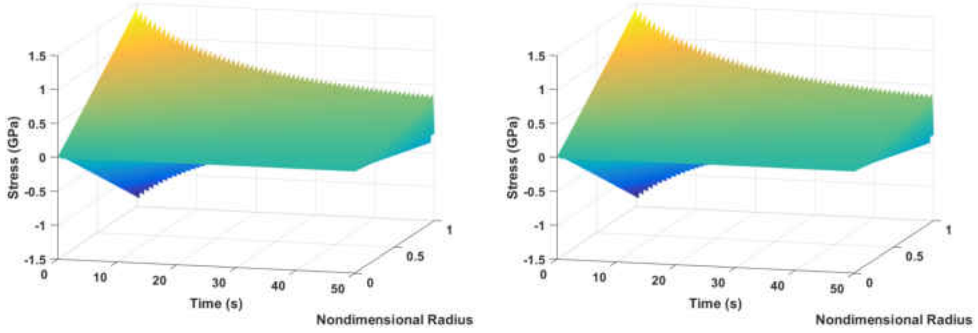

(a) $T = 298\,\mathrm{K}$ (b) $T = 303\,\mathrm{K}$

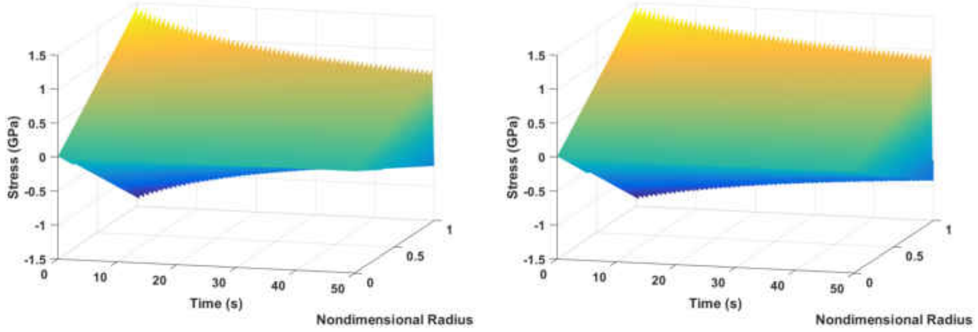

(c) $T = 343\,\mathrm{K}$ (d) $T = 403\,\mathrm{K}$

Figure 4.21: Bilinear Shear Stress Plots for Various Temperatures

It is also prudent to examine the evolution of the critical radius over time for various temperatures. Figures 4.22 represent these changes in the critical radius. The convergence in the lower limit changes with varying temperature, but not as severely as with changes in u_0, which implies that the initial displacement plays a much greater role in the shape of the critical radius lower limit. The temperature does play a significant role in the convergence value. When $T = 298\,\mathrm{K}$, the critical radius ratio lower limit is approximately $\delta_T \approx 0.16$ near the $50\,\mathrm{s}$ mark, but the ratio is much larger at $\delta_T \approx 0.56$ for a larger temperature of $T = 403\,\mathrm{K}$. Again, the critical radius is a function of the temperature via the critical shear stress, so it is expected for r_T to be larger in general for all martensite fractions and displacements.

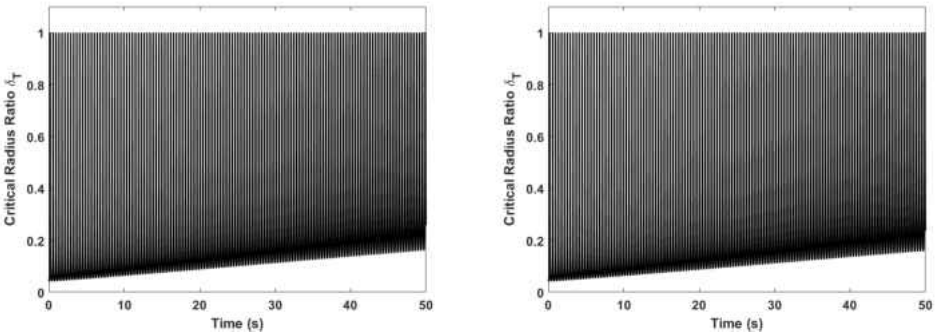

(a) $T = 298\,\mathrm{K}$ (b) $T = 303\,\mathrm{K}$

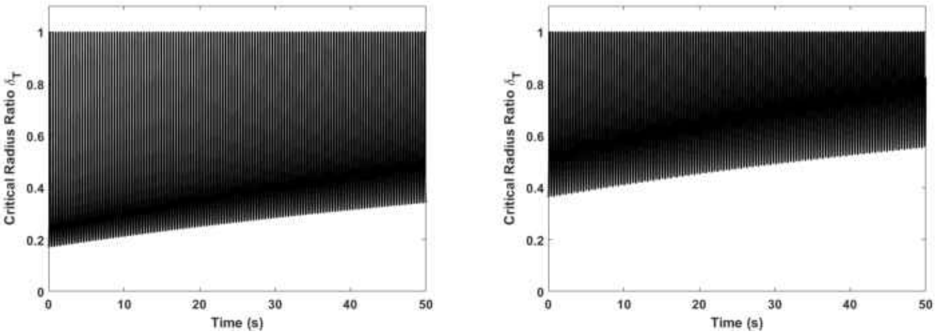

(c) $T = 343\,\mathrm{K}$ (d) $T = 403\,\mathrm{K}$

Figure 4.22: Critical Radius Plots for Various Temperatures

CHAPTER 5: CONCLUSION

In general, the bilinear assumption provides reasonable solutions to the SMA-spring-mass system's dynamics, since it matches the key assumptions better than the homogeneous case. In particular, the force-displacement plots for the bilinear case provide a shape that is analogous to the stress-strain diagram for the pseudoelastic effect. The bilinear case also offers a shear stress that is nonlinear, which is also a practical assumption. While the true stress state is mostly likely highly nonlinear, a piecewise function comprised of two straight line segments is a decent assumption that is more correct than a purely linear stress over the SMA wire's cross section. It is also interesting to note that the numerical solution of the bilinear case was quicker than the homogeneous case. This observation may be the result of the existence of the critical radius, where the martensite fractions past r_T have fixed values and are therefore computationally cheaper than solving for the martensite fractions at each every radial point.

In addition to the bilinear assumption providing reasonable results, the homogeneous approach presents rather odd results under certain conditions, and does not meet all of the key assumptions at all times. The only assumption met for all the conditions was the first one, that the displacement and velocity converge to zero. For the lower two temperatures assuming a homogeneous distribution, the martensite phase fraction plots showed that the twinned martensite fraction β_4, which is associated with heating and cooling, has non-zero values, when it should ideally equal zero for all time. For the largest initial displacement, β_1 and β_2 do not “trade off” each other. It would be nonsensical for a spring to experience both positive and negative stress at the same time, yet this was seen for the largest initial displacement. One final validation of the bilinear assumption over the homogeneous case is that the displacement for the largest initial displacement in the homogeneous case follows a highly nonlinear trend and converges to a value other than the equilibrium point. While there is merit in using the homogeneous case as an acceptable system approximation, this assumption can only model the system dynamics for so many conditions. When the homogeneous case fails, the bilinear case can provide a reasonable model.

There are, however, limits to the bilinear case as well. These limits seem to arrive mostly when considering the temperature. For instance, when the operating temperature is equal to or lower than the martensite start temperature, the force-displacement plot should not follow the pseudoelastic effect as seen in Fig. 1.3, in light of the stress-temperature plot in Fig. 1.4. The force-displacement plot should instead resemble something like the shape memory effect in Fig. 1.2, where the SMA oscillates on the unloading path as opposed to returning to its original configuration on the heating path. This limitation suggests that while the bilinear case may account for many more conditions than the homogeneous approach, the bilinear assumption is still limited in the number of conditions for which it can account.

With these limitations in mind, there are multiple areas for future research. One approach is to refine the critical shear stress model. The normal stress used to determine the shear stress corresponds to another model where the martensite-fractions evolution is not defined by differential equations. Perhaps the updated critical stress can offer vastly different solutions when the temperature is at or below the martensite start temperature. Another way of eliminating or reducing these restrictions is by assuming a completely nonlinear martensite-fractions assumption. For a fully nonlinear model, it cannot be assumed that the martensite fractions are independent of the radius within the SMA cross section, like in the homogeneous and (to some extent) bilinear assumptions. The goal of this branch on the research is to find a relation between the radius and the martensite fractions, something that may be best left to a material scientist.

In addition to the above potential corrections, another aim of future research is to make the single degree of freedom system more complex. What is the response of the system when acted upon by an applied force? Will the displacement change by a significant factor if friction were added to the model? How much more damping is recorded if an external damper is added to the system? Rather than considering a single degree of freedom system, future research can focus on a multiple degree of freedom system. What is the impact of the damping on all masses in a multiple degree of freedom system if just one spring were replaced by an SMA? What sort of martensite-fractions evolution would one see in a rigid, continuous body attached to a base by a spring?

One last branch of research involves experimental testing. While the bilinear case seems like an improvement over the homogeneous case, the bilinear case may not actually match the true system dynamics. An investigation that collects experimental data can be comprised of a small car on a track connected to a base by an SMA spring. Researchers can place an accelerometer on the car to obtain the car's displacement and velocity, as well as add a force gage and record the force. If the resulting data correlate well with a certain assumption, particularly the bilinear assumption, then that model is a good fit of the data. For comparison, the study can also include collecting data for a spring-mass system with a traditional spring. That way, one can determine whether the measured damping from an SMA spring is significantly greater than the damping of an ideal spring with friction acting on the system.

APPENDIX A: SMA SPRING PLOTTER CODE

```
%Mass-SMA Spring System Dynamics

tic

clear all; close all; clc;
set(0,'DefaultAxesFontSize',16,'DefaultTextFontSize',16,...
    'DefaultAxesFontName','Helvetica',...
    'DefaultTextFontName','Helvetica',...
    'DefaultAxesFontWeight','bold','DefaultTextFontWeight','
       bold',...
    'DefaultLineLineWidth',2,'DefaultLineMarkerSize',12,...
    'DefaultFigureColor','w','DefaultFigureResize','off',...
    'DefaultFigurePosition',[5 100 [900 650]*.9])

%Spring constant values
D = 6e-3;                   %Spring external diameter (m)
d = 0.75e-3;                %Wire diameter (m)
N = 20;                     %Number of active coils
T = 343;                    %Operation temperature (K)
c = 0;                      %External damping coefficient
m = 2.0;                    %System mass (kg)

%SMA constant values
GA = 14.5e9;                %Martensite Young's modulus (Pa)
GM = 11.5e9;                %Austenite Young's modulus (Pa)

%Paper constant values
a = 40e6;                   %Stress-strain hysteris loop height
    (Pa)
gR = 0.028;                 %Residual strain
TM = 303;                   %Stable martensitic phase
   temperature (K)

    %Critical Stress Phase Transformation
LM0 = 0.6e3;                %Martensite Constant (Pa)
LM = 29.5e6;                %Martensite Linear (Pa)
LA0 = 0.03e3;               %Austenite Constant (Pa)
LA = 48.5e6;                %Austenite Linear (Pa)

    %Internal Dissipation Parameters
h1L = 220e6;                %Upper 1 (Pa*s)
h1U = 20e6;                 %Lower 1 (Pa*s)
```

```
h2L = 220e6;                %Upper 2 (Pa*s)
h2U = 20e6;                 %Lower 2 (Pa*s)
h3L = 220e6;                %Upper 3 (Pa*s)
h3U = 23e6;                 %Lower 3 (Pa*s)

h1 = h1L;                   %The values h1, h2, and h3 are for
   the
h2 = h2L;
h3 = h3L;

%Intermediate Calculations and Definitions
ah = gR-a/GM;               %Stress-strain hysteresis loop
   parameter

L1 = -LM0+LM/TM*(T-TM);     %Critical stress parameter (Pa)
L2 = L1;                    %Critical stress parameter (Pa)
L3 = -LA0+LA/TM*(T-TM);     %Critical stress parameter (Pa)
L = [L1;L2;L3];             %Critical stress parameter vector

Smins = 100e6;              %Minimum martensite critical stress
    (Pa)
CM = 8e6;                   %Temperature Stress Parameter (Pa/C
   )

if T < TM
    SMS = Smins;
else
    SMS = Smins+CM*(T-TM);
end

tcrit = (1/sqrt(3))*SMS;

%Initial conditions
u0 = 2.00; ud0 = 0;         %Initial displacement and velocity
b10 = 0; b20 = 0; b30 = 1;  %Initial martensite fractions
y0 = [u0,ud0,b10,b20,b30]'; %Inital conditions matrix

%Split Iteration
dr = (5e-5)*(d/2);          %Radius step size
r = 0:dr:d/2;               %Radius vector (m)
Nr = length(r);             %Radius vector length
dt = 0.01;                  %Time step size (s)
```

```
TT = 0:dt:50;                    %Time vector (s)
NTT = length(TT);
y = y0;

%Martensite Case Parameter Vectors
p1 = [d,D,a,ah,c,GA,GM,N,m];%Parameter vector 1

assume = input('Type 0 for Homogeneous or 1 for Bilinear: ');
switch assume
    case 0                  %Homogeneous Case
        tcrit = 0;
    case 1                  %Bilinear Case

    otherwise
        tcrit = disp('Error');
end
for n = 1:NTT
    %Ya Runge-Kutta Calcs
    ya = y(1:2);

    k = Force(y,dt,p1,tcrit);
    ya = ya+k;
    u = ya(1); ud = ya(2);
    G = GM+y(5)*(GA-GM);
    rT = abs((pi*D^2*N)/(2*G*u)*tcrit);
    delT = 2*rT/d;

    if delT >= 1
        delT = 1;
        rT = d/2;
        b1 = 0; b2 = 0; b3 = 1;
        for j = 1:Nr
            tau(j,n) = GA*2*r(j)/(pi*D^2*N)*u;
        end
        yb = [b1;b2;b3];

    else

        if ud > 0
            h1 = h1L; h2 = h2L; h3 = h3L;
        end
```

```
if ud < 0
    h1 = h1U; h2 = h2U; h3 = h3U;
end

%Yb1 Calcs
for j = 1:Nr

    if r(j) <= rT
        b1 = 0;
        b2 = 0;
        b3 = 1;
    else

        b1 = y(3); b2 = y(4); b3 = y(5);

        G = GM+b3*(GA-GM);
        g = (2*r(j))/(pi*D^2*N)*u;
        %rT = abs((pi*D^2*N)/(2*G*u)*tcrit);
        b1 = b1+(dt/h1)*((a+G*ah)*g+L1+(2*ah*a+G*ah^2)
           *(b2-b1));
        b2 = b2+(dt/h2)*(-(a+G*ah)*g+L2-(2*ah*a+G*ah^2)
           *(b2-b1));
        b3 = b3+(dt/h3)*(-0.5*(GA-GM)*(g+ah*(b2-b1))
           .^2+L3);

        %Internal Martensite Constraints (Jpi)
        yb = Tetra(b1,b2,b3);
        b1 = yb(1); b2 = yb(2); b3 = yb(3);

        %Internal Sub-loop Constraints (Jchi)
        g = (2*r(j))/(pi*D^2*N)*u;
        yb1(:,n) = yb;
        gs(n) = g;

        if n > 1
            db = (yb-yb1(:,n-1))/dt;
            dg = (g-gs(:,n-1))/dt;
            yb = J_Chi(g,yb,db,yb1(:,n-1),dg);
            b1 = yb(1); b2 = yb(2); b3 = yb(3);

        end
```

```
        end

        b1v(j) = b1;
        b2v(j) = b2;
        b3v(j) = b3;

        switch assume
            case 0
                tau(j,n) = (GM+b3*(GA-GM))*2*r(j)/(pi*D^2*N
                   )*u+...
                (a+(GM+b3v(j)*(GA-GM))*ah)*(b2-b1);
            case 1
                if r(j) <= rT
                    tau(j,n) = GA*2*r(j)/(pi*D^2*N)*u;
                else
                    tau(j,n) = (GM+b3*(GA-GM))*2*r(j)/(pi*D
                       ^2*N)*u+...
                    (a+(GM+b3v(j)*(GA-GM))*ah)*(b2-b1);
                end
        end

    end

    Ar = (d/2)^2;
    b1avg = 2*r*b1v'*dr/Ar;             %Compile across
       cross-section
    b2avg = 2*r*b2v'*dr/Ar;
    b3avg = 2*r*b3v'*dr/Ar;

    jrT = find(r<=rT); jrT = jrT(end);

    b1avg = b1avg*Ar/((d/2)^2-rT^2);    %Compile past
       critical radius
    b2avg = b2avg*Ar/((d/2)^2-rT^2);
    b3avg = (b3avg*Ar-2*dr*sum(r(1:jrT)))/((d/2)^2-rT^2);

    yb = [b1avg;b2avg;b3avg];

end

%Compiling Ya and Yb
y = [ya;yb];
```

```
    yp(:,n) = y;

end

toc

%Calculating Extra Variables
    %Defining the State Variables
u = yp(1,:); ud = yp(2,:);
b1 = yp(3,:); b2 = yp(4,:); b3 = yp(5,:); b4 = 1-b1-b2-b3;
bsum = b1+b2+b3+b4;

    %Defining other Variables
G = GM+b3*(GA-GM);

    %Assumption specific variables
switch assume
    case 0
        delT = 0;
    case 1
        rT = abs((pi*D^2*N)./(2.*G.*u).*tcrit);
        delT = 2*rT/d;

        for n = 1:NTT
            if rT(n) >= d/2
                rT(n) = d/2; delT(n) = 2*rT(n)/d;
            end
        end
end

F = pi*d^3/(8*D)*((d/(pi*D^2*N))*G.*u+...
    (4/3)*(a+G*ah).*(b2-b1).*(1-delT.^3));

%Response Plot
figure;
subplot(2,1,1); plot(TT,u,'k');
xlabel('Time (s)'); ylabel('Displacement (m)');
subplot(2,1,2); plot(TT,ud,'k');
xlabel('Time (s)'); ylabel('Velocity (m/s)');

%Phase Plot
figure;
```

```
plot(u,ud,'k');
xlabel('Displacement (m)');
ylabel('Velocity (m/s)');

%Martensite Fraction Plot
figure;
plot(TT,b1,'k',TT,b2,'b',TT,b3,'r',TT,b4,'g');
xlabel('Time (s)'); ylabel('Martensite Fraction');
legend('\beta_1','\beta_2','\beta_3','\beta_4');
ylim([-0.2 1.2]);

%Force-Displacement Plot
figure;
plot(u,F,'k');
xlabel('Displacement (m)');
ylabel('Restoring Force (N)');

%Shear Stress Plot
figure;
tau_s=tau(1:200:end,:);
surf(TT,(2/d)*r(1:200:end),tau_s*1e-9); shading flat;
xlabel('Time (s)'); ylabel('Nondimensional Radius'); zlabel('
   Stress (GPa)');
view(15,15);

%Critical Radius Plot
switch assume
    case 1
        figure;
        plot(TT,delT,'k');
        xlabel('Time (s)');
        ylabel('Critical Radius Ratio \delta_T');
        ylim([0 1.1]);
end
```

APPENDIX B: FORCE CODE

```
function [k] = Force(y,dt,p,tcrit)

d = p(1); D = p(2); a = p(3);
ah = p(4); c = p(5); GA = p(6);
GM = p(7); N = p(8); m = p(9);

%Intermediate Values
A = pi*d^3/(8*D);
B = d/(pi*D^2*N);

%Differential Spring Mass Equations
x = y;

G = GM+x(5)*(GA-GM);
rT = abs((pi*D^2*N)/(2*G*x(1))*tcrit);
delT = 2*rT/d;

if delT >= 1
    delT = 1;
    x(3) = 0; x(4) = 0; x(5) = 1;
end

FF = A*((B*G*x(1)+(4/3)*(a+G*ah)*(x(4)-x(3))*(1-delT)^3));
F = [x(2);-c/m*x(2)-FF/m];
k1 = dt*F;
x = y+1/2*[k1;0;0;0];

G = GM+x(5)*(GA-GM);
rT = abs((pi*D^2*N)/(2*G*x(1))*tcrit);
delT = 2*rT/d;

if delT >= 1
    delT = 1;
    x(3) = 0; x(4) = 0; x(5) = 1;
end

FF = A*((B*G*x(1)+(4/3)*(a+G*ah)*(x(4)-x(3))*(1-delT)^3));
F = [x(2);-c/m*x(2)-FF/m];
k2 = dt*F;
x = y+1/2*[k2;0;0;0];

G = GM+x(5)*(GA-GM);
```

```
rT = abs((pi*D^2*N)/(2*G*x(1))*tcrit);
delT = 2*rT/d;

if delT >= 1
    delT = 1;
    x(3) = 0; x(4) = 0; x(5) = 1;
end

FF = A*((B*G*x(1)+(4/3)*(a+G*ah)*(x(4)-x(3))*(1-delT)^3));
F = [x(2);-c/m*x(2)-FF/m];
k3 = dt*F;
x = y+[k3;0;0;0];

G = GM+x(5)*(GA-GM);
rT = abs((pi*D^2*N)/(2*G*x(1))*tcrit);
delT = 2*rT/d;

if delT >= 1
    delT = 1;
    x(3) = 0; x(4) = 0; x(5) = 1;
end

FF = A*((B*G*x(1)+(4/3)*(a+G*ah)*(x(4)-x(3))*(1-delT)^3));
F = [x(2);-c/m*x(2)-FF/m];
k4 = dt*F;

k = 1/6*(k1+2*k2+2*k3+k4);

end
```

APPENDIX C: CORRECT CODE

```matlab
function [yb] = Correct(a,b)

if (a >= 0) && (b >= 0) && (a+b <= 1)
    dy3 = 0; dy4 = 0;

    a = a+dy3; b = b+dy4;

else
    if a < 0
        dy3 = -a; dy4 = 0;
        a = a+dy3; b = b+dy4;
    end

    if b < 0
        dy3 = 0; dy4 = -b;
        a = a+dy3; b = b+dy4;
    end

    if b <= a-1
        dy3 = 1-a; dy4 = -b;
        a = a+dy3; b = b+dy4;
    end

    if (a > 0) && (b > 0) && (b > a-1) && (b < a+1)
        dy3 = (1-a-b)/2; dy4 = dy3;
        a = a+dy3; b = b+dy4;
    end

    if b >= a+1
        dy3 = -a; dy4 = 1-b;
        a = a+dy3; b = b+dy4;
    end

end

yb = [a;b];

end
```

APPENDIX D: TETRA CODE

```
function [yb] = Tetra(a,b,c)

if (a >= 0) && (b >= 0) && (c >= 0) && (a+b+c <= 1)
    dy3 = 0; dy4 = 0; dy5 = 0;


    a = a+dy3; b = b+dy4; c = c+dy5;

else
    if (c < 0) || ((a >= 0) && (b >= 0) && (c >= 0) && (c <=
       0.5*(a+b-1)))
        dy5 = -c;
        dy = Correct(a,b);
        a = dy(1); b = dy(2); c = c+dy5;
    end

    if (a < 0) || ((a >= 0) && (b >= 0) && (c >= 0) && (a <=
       0.5*(b+c-1)))
        dy3 = -a;
        dy = Correct(b,c);
        a = a+dy3; b = dy(1); c = dy(2);
    end

    if (b < 0) || ((a >= 0) && (b >= 0) && (c >= 0) && (b <=
       0.5*(c+a-1)))
        dy4 = -b;
        dy = Correct(c,a);
        a = dy(2); b = b+dy4; c = dy(1);
    end

    if (a > 0) && (b > 0) && (c > 0) && (c > 0.5*(a+b-1)) &&...
            (a > 0.5*(b+c-1)) && (b > 0.5*(c+a-1))
        dy3 = (1-a-b-c)/3; dy4 = dy3; dy5 = dy4;
        a = a+dy3; b = b+dy4; c = c+dy5;
    end
end

yb = [a;b;c];

end
```

APPENDIX E: J CHI CODE

```
function [yb] = J_Chi(g,yb,bd,yb1,gd)

b1 = yb(1); b2 = yb(2); b3 = yb(3);
b1d = bd(1); b2d = bd(2); b3d = bd(3);

if g > 0
    if gd*b1d < 0
        if abs(gd) >= abs(b1d)
            b1 = yb1(1);
        end
    end

    if gd*b3d > 0
        if abs(gd) >= abs(b3d)
            b3 = yb1(3);
        end
    end
end

if g < 0
    if gd*b2d > 0
        if abs(gd) >= abs(b2d)
            b2 = yb1(2);
        end
    end

    if gd*b3d < 0
        if abs(gd) >= abs(b3d)
            b3 = yb1(3);
        end
    end
end

yb = [b1;b2;b3];

end
```

LIST OF REFERENCES

[1] D. J. Leo, *Engineering analysis of smart material systems.* John Wiley & Sons, 2007.

[2] B. Carpenter and J. Lyons, “Lightweight flexible solar array validation report,” *EO-1 First, NASA mission, validation report*, 2002.

[3] A. Czechowicz and S. Langbein, *Shape memory alloy valves: Basics, potentials, design.* Springer, 2015.

[4] C. Liang and C. Rogers, “Design of shape memory alloy springs with applications in vibration control,” *Journal of Intelligent Material Systems and Structures*, vol. 8, no. 4, pp. 314–322, 1997.

[5] K. Tanaka, S. Kobayashi, and Y. Sato, “Thermomechanics of transformation pseudoelasticity and shape memory effect in alloys,” *International Journal of Plasticity*, vol. 2, no. 1, pp. 59–72, 1986.

[6] L. Brinson and M. Huang, “Simplifications and comparisons of shape memory alloy constitutive models,” *Journal of intelligent material systems and structures*, vol. 7, no. 1, pp. 108–114, 1996.

[7] X. Zhang, C. Rogers, and C. Liang, “Modelling of the two-way shape memory effect,” *Journal of intelligent material systems and structures*, vol. 8, no. 4, pp. 353–362, 1997.

[8] J. H. Mabe, F. T. Calkins, and M. B. Alkislar, “Variable area jet nozzle using shape memory alloy actuators in an antagonistic design,” in *Industrial and Commercial Applications of Smart Structures Technologies 2008*, vol. 6930. International Society for Optics and Photonics, 2008, p. 69300T.

[9] M. Tawfik, J.-J. Ro, and C. Mei, “Thermal post-buckling and aeroelastic behaviour of shape memory alloy reinforced plates,” *Smart Materials and Structures*, vol. 11, no. 2, pp. 297–307, 2002.

[10] H. Li, M. Liu, and J. Ou, “Vibration mitigation of a stay cable with one shape memory alloy damper,” *Structural Control and Health Monitoring*, vol. 11, no. 1, pp. 21–36, 2004.

[11] Y. Sakai, Y. Kitagawa, T. Fukuta, and M. Iiba, “Experimental study on enhancement of self-restoration of concrete beams using sma wire,” in *Smart Structures and Materials 2003: Smart Systems and Nondestructive Evaluation for Civil Infrastructures*, vol. 5057. International Society for Optics and Photonics, 2003, pp. 178–187.

[12] S. Pittaccio and S. Viscuso, “An emg-controlled sma device for the rehabilitation of the ankle joint in post-acute stroke,” *Journal of materials engineering and performance*, vol. 20, no. 4-5, pp. 666–670, 2011.

[13] C. Liang and C. Rogers, “Design of shape memory alloy actuators,” *Journal of Intelligent Material Systems and Structures*, vol. 8, no. 4, pp. 303–313, 1997.

[14] D. C. Lagoudas, T. Kalmar-Nagy, and M. Z. Lagoudas, “Shape memory alloys for vibration isolation and damping of large-scale space structures,” TEXAS A AND M UNIV COLLEGE STATION, Tech. Rep., 2010.

[15] J. E. Shigley, “Mechanical engineering design,” 1972.

[16] R. A. Aguiar, M. A. Savi, and P. M. Pacheco, “Experimental and numerical investigations of shape memory alloy helical springs,” *Smart Materials and Structures*, vol. 19, no. 2, p. 025008, 2010.

[17] V. C. de Sousa, C. D. M. Junior, and M. Elahinia, “Aeroelastic behavior of a typical section with shape memory alloy springs: Modeling nonhomogeneous distribution of state variables,” *Applied Mathematical Modelling*, vol. 52, pp. 404–416, 2017.

[18] K. Tanaka and S. Nagaki, “A thermomechanical description of materials with internal variables in the process of phase transitions,” *Ingenieur-Archiv*, vol. 51, no. 5, pp. 287–299, 1982.

[19] C. Liang and C. A. Rogers, “One-dimensional thermomechanical constitutive relations for shape memory materials,” *Journal of intelligent material systems and structures*, vol. 8, no. 4, pp. 285–302, 1997.

[20] L. C. Brinson, “One-dimensional constitutive behavior of shape memory alloys: thermomechanical derivation with non-constant material functions and redefined martensite internal variable,” *Journal of intelligent material systems and structures*, vol. 4, no. 2, pp. 229–242, 1993.

[21] M. Fremond, “Matériaux à mémoire de forme,” *Comptes rendus de l’Académie des sciences. Série 2, Mécanique, Physique, Chimie, Sciences de l’univers, Sciences de la Terre*, vol. 304, no. 7, pp. 239–244, 1987.

[22] M. Savi and A. Braga, “Chaotic vibrations of an oscillator with shape memory,” *J. Braz. Soc. Mech. Sci. Eng*, vol. 15, no. 1, pp. 1–20, 1993.

[23] M. A. Savi, A. Paiva, A. P. Baêta-Neves, and P. M. Pacheco, “Phenomenological modeling and numerical simulation of shape memory alloys: a thermo-plastic-phase transformation coupled model,” *Journal of Intelligent Material Systems and Structures*, vol. 13, no. 5, pp. 261–273, 2002.

[24] A. P. Baêta-Neves, M. A. Savi, and P. M. Pacheco, "On the fremond's constitutive model for shape memory alloys," *Mechanics Research Communications*, vol. 31, no. 6, pp. 677–688, 2004.

[25] A. Paiva, M. A. Savi, A. M. B. Braga, and P. M. C. L. Pacheco, "A constitutive model for shape memory alloys considering tensile–compressive asymmetry and plasticity," *International Journal of Solids and Structures*, vol. 42, no. 11-12, pp. 3439–3457, 2005.

[26] M. Savi and A. Paiva, "Describing internal subloops due to incomplete phase transformations in shape memory alloys," *Archive of Applied Mechanics*, vol. 74, no. 9, pp. 637–647, 2005.

[27] H. Tobushi and K. Tanaka, "Deformation of a shape memory alloy helical spring: Analysis based on stress-strain-temperature relation," *JSME international journal. Ser. 1, Solid mechanics, strength of materials*, vol. 34, no. 1, pp. 83–89, 1991.

[28] M. A. Savi and A. M. Braga, "Chaotic response of a shape memory oscillator with internal constraints," in *Proceedings of the 12th Brazilian Congress of Mechanical Engineering*, 1993, pp. 33–36.

[29] M. Ortiz, P. M. Pinsky, and R. L. Taylor, "Operator split methods for the numerical solution of the elastoplastic dynamic problem," *Computer Methods in Applied Mechanics and Engineering*, vol. 39, no. 2, pp. 137–157, 1983.

[30] A. J. Chorin, T. J. Hughes, M. F. McCracken, and J. E. Marsden, "Product formulas and numerical algorithms," *Communications on Pure and Applied Mathematics*, vol. 31, no. 2, pp. 205–256, 1978.